West African Monsoon System's Responses to Global Ocean–Regional Atmosphere Coupling

ALAIN T. TAMOFFO,[a] TORSTEN WEBER,[a] WILLIAM CABOS,[b] PAUL-ARTHUR MONERIE,[c] KERRY H. COOK,[d] DMITRY V. SEIN,[e,f] ALESSANDRO DOSIO,[g] NANA A. B. KLUTSE,[h,i] AKINTOMIDE A. AKINSANOLA,[j,k] AND DANIELA JACOB[a]

[a] *Climate Service Center Germany (GERICS), Helmholtz-Zentrum Hereon, Hamburg, Germany*
[b] *Departamento de Física y Matemáticas, Universidad de Alcalá, Alcalá de Henares, Madrid, Spain*
[c] *National Centre for Atmospheric Science, Reading, United Kingdom*
[d] *Department of Geological Sciences, Jackson School of Geosciences, The University of Texas at Austin, Austin, Texas*
[e] *Alfred Wegener Institute for Polar and Marine Research, Bremerhaven, Germany*
[f] *Shirshov Institute of Oceanology, Russian Academy of Science, Moscow, Russia*
[g] *European Commission, Joint Research Centre, Ispra, Italy*
[h] *African Institute for Mathematical Sciences, Kigali, Rwanda*
[i] *Department of Physics, University of Ghana, Accra, Ghana*
[j] *Department of Earth and Environmental Sciences, University of Illinois Chicago, Chicago, Illinois*
[k] *Environmental Science Division, Argonne National Laboratory, Lemont, Illinois*

(Manuscript received 18 December 2023, in final form 2 May 2024, accepted 14 May 2024)

ABSTRACT: This study explores the added value (AV) of a regional Earth system model (ESM) compared to an atmosphere-only regional climate model (RCM) in simulating West African monsoon (WAM) rainfall. The primary goals are to foster discussions on the suitability of coupled RCMs for WAM projections and deepen our understanding of ocean–atmosphere coupling's influence on the WAM system. The study employs results from dynamical downscaling of the ERA-Interim reanalysis and Max Plank Institute ESM, low resolution (MPI-ESM-LR), by two RCMs, atmosphere only (REMO) and REMO coupled with Max Planck Institute Ocean Model (MPIOM) (ROM), at ~25-km horizontal resolution. Results show that in regions distant from coupling domain boundaries such as West Africa (WA), constraint conditions from ERA-Interim are more beneficial than coupling effects. REMO, reliant on oceanic sea surface temperatures (SSTs) from observations and influenced by ERA-Interim, is biased under coupling conditions, although coupling offers potential advantages in representing heat and mass fluxes. Contrastingly, as intended, coupling improves SSTs and monsoon fluxes' relationships under ESM-forced conditions. In this latter case, the coupling features a dipole-like spatial structure of AV, improving precipitation over the Guinea Coast but degrading precipitation over half of the Sahel. Our extensive examination of physical processes and mechanisms underpinning the WAM system supports the plausibility of AV. Additionally, we found that the monsoonal dynamics over the ocean respond to convective activity, with the Sahara–Sahel surface temperature gradient serving as the maintenance mechanism. While further efforts are needed to enhance the coupled RCM, we advocate for its use in the context of WAM rainfall forecasts and projections.

KEYWORDS: Atmosphere-ocean interaction; Atmospheric circulation; Monsoons; Climate models; Coupled models; Regional models

1. Introduction

There is a growing need to find solutions to improve weather forecasts and climate projections to accurately design society's responses to climate change–related hazards [IPCC's Sixth Assessment Report, chapter 10 (AR6 Ch10); Doblas-Reyes et al. 2021]. This statement is more relevant in a context where, for instance, the high variability of West African monsoon (WAM) rainfall and extreme events has strong societal impacts. Despite this, significant biases still exist in the WAM system simulations (e.g., Boone et al. 2010; Diallo et al. 2014). The dynamical downscaling approach is undeniably part of the solution to improving the numerical representation of the African climate system. It excels in providing superior resolution of orography over land, air–sea interactions, land processes (e.g., albedo, land cover, sharp gradients in temperature, and soil moisture), potential vorticity, influence of lakes, and weather fronts, which aspects are not resolved by global models (Jacob and Podzun 1997; Feser 2006; Paeth and Mannig 2012). It, indeed, proved its effectiveness in recent decades by providing substantial added value in simulating the African climate system (e.g., Dosio et al. 2015; Paxian et al. 2016; Gibba et al. 2019; Wu et al. 2020). However, significant biases, both those stemming from the regional climate model (RCM) and those inherited from boundary conditions, along with inconsistencies (lack of

Denotes content that is immediately available upon publication as open access.

Supplemental information related to this paper is available at the Journals Online website: https://doi.org/10.1175/JCLI-D-23-0749.s1.

Corresponding author: Alain T. Tamoffo, alain.tamoffo@hereon.de

DOI: 10.1175/JCLI-D-23-0749.1

shared internal physics and configurations) between the driving Earth system models (ESMs) and RCMs used for the downscaling, have the potential to lead to spurious results in the dynamical downscaling (Laprise et al. 2013; Panitz et al. 2014; Saini et al. 2015). Especially over West Africa (WA), a prominent hotspot for climate change on the continent (Martin and Thorncroft 2014), where the range in projected changes rivals the extent of biases in RCMs (Bichet et al. 2020; Monerie et al. 2020; Zhou et al. 2020). This poses a critical concern with regard to the reliability of forecasts and projections, especially in a region where the monsoon system not only determines the timing but also has the potential to alter the efficiency of economic activities (Niang et al. 2014). Hence, the objective of the current study is to assess the efficiency of a relatively underutilized dynamical downscaling approach proposed by Sein et al. (2015) in accurately simulating the WAM system. This approach involves coupling a global ocean model with a stand-alone atmosphere-only RCM to enable interactive sea surface temperatures (SSTs).

Improving the understanding of the WAM system's functioning, and subsequently, improving forecasts and projections, has motivated numerous international research programs and field campaign studies. For example, the African Multidisciplinary Monsoon Analysis Model Intercomparison Project (AMMA-MIP; Redelsperger et al. 2006) and the AMMA Land Surface Model Intercomparison Project (ALMIP; Boone et al. 2009) were dedicated to this endeavor. Notable progress has been achieved in refining climate models to better represent land–atmosphere coupling through initiatives such as the West African Monsoon Modeling and Evaluation (WAMME; Boone et al. 2010) project. The WA region has also garnered substantial research attention through various phases of the Coupled Model Intercomparison Projects (CMIPs; Meehl et al. 2007; Taylor et al. 2012; Eyring et al. 2016) and the Coordinated Regional Climate Downscaling Experiment (CORDEX) project (Gutowski et al. 2016). These concerted efforts have significantly contributed to addressing uncertainties in the historical and projected climatology of WAM precipitation (e.g., Druyan et al. 2010; Diallo et al. 2016; Akinsanola et al. 2018; Akinsanola and Zhou 2019; Dosio et al. 2020; Tamoffo et al. 2023a,b). However, studies conducted within the aforementioned programs showed that much work still needs to be done to reduce biases, which is crucial for enhancing confidence in future projections (e.g., Paeth et al. 2005; Boone et al. 2009, 2010; Hourdin et al. 2010; Xue et al. 2010).

While dynamical downscaling based on stand-alone atmosphere-only RCMs is considerably suitable in better capturing smaller-scale physiographic processes and mesoscale convective systems, it is not sufficient to address the biases present in ESMs. This may suggest that the downscaling approach reliant on imposing SSTs onto RCMs may not be the optimal method, and exploring better alternatives could be more beneficial. Previous studies (e.g., Sein et al. 2014, 2015; Zou and Zhou 2016; Samanta et al. 2018) have indicated that models with interactive computational SSTs at high horizontal resolution are better suited for simulating climate systems characterized by strong ocean–atmosphere interactions. This perspective gains more relevance in the context of monsoon systems, which typically respond to changes in land–sea thermal/pressure contrasts. Modeling of monsoon systems using such coupled ocean–atmosphere RCMs has prompted numerous investigations. For instance, Zou and Zhou (2016) demonstrated that the regional ocean–atmosphere coupled model FROALS accurately represents the East Asia monsoon system, particularly due to a reduction in SST biases. Similarly, in Central India, an ocean mixed layer model coupled with an RCM significantly alleviated the dry bias observed in the atmospheric component's simulation. This improvement was attributed to enhanced simulations of horizontal and vertical shears, which responded to improvements in the coastal SST front over the Bay of Bengal (Samanta et al. 2018). Over southern Africa, a comparison between coupled and uncoupled RCMs revealed that air–sea feedback is relevant for modeling precipitation during the rainfall maximum, largely due to the strong involvement of tropical processes (e.g., SST variability, moisture transport, and Walker- and Hadley-like circulations); however, this is not the case during the onset phases of precipitation (Ratnam et al. 2015).

A preliminary investigation conducted by Paxian et al. (2016) highlighted, among other hypotheses, that employing dynamical downscaling with an RCM coupled to a global ocean model can improve the representation of WAM rainfall. The authors showed that such coupling diminishes the Atlantic SST bias, resulting in a more accurate representation of air–sea interactions. The reduction in SST bias triggers improvements in ocean currents, particularly the coastal upwelling of the Benguela and warm Angola currents. Consequently, the resulting atmospheric circulation is enhanced, leading to improvements in precipitation over the tropical Atlantic, Guinea Gulf, Guinea Coast, and Central Sahel.

The objective of our present study builds upon the aforementioned perspectives while seeking a deeper understanding of how the ocean–atmosphere coupling modulates the monsoon system, at both the mesoscale and local scales. We aim to highlight a chain of underlying processes that differentiate between coupled and uncoupled RCMs in the WAM rainfall climatology. Unlike previous studies that utilized a similar approach, primarily focusing on the SSTs (e.g., Paxian et al. 2016), our study provides the first assessment of the impacts of coupling a global ocean model to an atmospheric RCM on the simulation of WAM rainfall and the underlying local and regional forcing factors. This novel approach allows us, first, to assess the potential added value provided by the ocean–atmosphere coupled approach in comparison with the uncoupled approach. This assessment will stimulate discussions on the appropriateness of adopting coupled RCMs instead of atmosphere-only RCMs for projection purposes within the WAM system. Second, this approach will enable us to gain deeper insights into how SSTs drive the monsoon convective system, if at all, and how the monsoon convective system triggers oceanic responses (Birch et al. 2014).

The remainder of the document is structured as follows: In section 2, experimental, observational, and reanalysis data and the methods used in this study are introduced. Section 3 examines the differences between coupled and uncoupled RCMs of rainfall climatology and associated added value. In section 4, processes driving the differences described in section 3 are investigated and the plausibility of added value

TABLE 1. Details of forcing data and names of RCM experiments used in this study.

Institution	ESMs' names	RCMs (0.22° × 0.22°)	Experiment names	Ocean atmosphere	Periods used	Reference
ECMWF	ERA-Interim (0.75° × 0.75°)	REMO	REMO-ERA	Uncoupled	1980–2005	Dee et al. (2011)
		ROM	ROM-ERA	Coupled		
Max Planck Institute for Meteorology	MPI-ESM-LR (1.9° × 1.9°)	REMO	REMO-MPI-ESM-LR	Uncoupled	1980–2005	Stevens et al. (2013)
		ROM	ROM-MPI-ESM-LR	Coupled		

derived from the coupling is highlighted. Section 5 provides a discussion and concludes the paper.

2. Data and methods

a. Data

Model data utilized in this study are from a dynamical downscaling of the European Centre for Medium-Range Weather Forecasts (ECMWF) ERA-Interim reanalysis data (Dee et al. 2011) and the Max Plank Institute ESM, low resolution (MPI-ESM-LR; Stevens et al. 2013). ERA-Interim and MPI-ESM-LR provide lateral boundary conditions for the evaluation and historical simulations, respectively. Further details on the two driving datasets and the names of the simulations stemming from each are presented in Table 1.

Two distinct regional climate models are used as the dynamical downscaling tools in this study. The first is the regional climate model REMO (Jacob 2001). REMO is an atmosphere-only RCM developed at the Max Planck Institute for Meteorology in Hamburg, Germany, and its maintenance is currently performed at the Climate Service Center Germany (GERICS). The second is the regionally coupled model ROM (Sein et al. 2015; Cabos et al. 2020), which is a combination of REMO as the atmospheric component and Max Planck Institute Ocean Model (MPIOM; Jungclaus et al. 2013) as the ocean component. Refer to Sein et al. (2015), Cabos et al. (2020), and Weber et al. (2023) for full details about the physical configurations of the global ocean–regional atmosphere coupled RCM–ROM used in the present study. Briefly, the ocean model underwent a two-cycle spinup, forced by the 1958–2002 ERA-Interim data, totaling 90 years. At the start of the spinup, the ocean is at rest, with its temperature and salinity derived from the Leviticus January climatology. Over these 90 years, the ocean velocities, salinity, and temperature for MPIOM are adjusted, reaching a state of quasi-equilibrium, especially in the upper ocean layers. The subsequent spinup of the coupled models ROM-ERA and ROM-MPI continued from the final state of the forced MPIOM run. The REMO-MPI setup underwent further spinup using the MPI-ESM-LR forcing data from 1950. Meanwhile, ROM-ERA was forced by reanalysis data from ERA-40 (1958–80) and ERA-Interim (1981–2002). During the coupled spinup, consideration was given to the prolonged thermohaline and dynamical adjustments, particularly in deeper layers. During the coupled spinup, special attention was paid to prolonged thermohaline and dynamical adjustments, particularly in deeper layers. For this reason, ROM-ERA underwent spinup first with ERA-Interim and then with ERA-40, as the warming trend observed during the 1981–2002 run rendered it unsuitable as the initial state for the production run. Instead, the ROM-ERA production run commenced from a state closer to observed conditions. The impact of forcing changes was deemed insignificant after 1 or 2 years, particularly in SSTs; therefore, the production run for the two setups commenced when the initial state approximated a quasi-equilibrium (with a realistic initial state for ROM-ERA), despite limitations in discarding initial years. As demonstrated by Paxian et al. (2016) in the context of decadal predictions, and by Sein et al. (2015) and Cabos et al. (2017) for historical simulations, the Atlantic SST bias is significantly reduced in coupled regional simulations. This reduction is attributed to the representation of fine-scale air–sea interactions at high atmosphere and ocean resolutions, which improve deficient GCM winds and surface ocean currents, intensify the cold water upwelling of the Benguela Current, and decrease the southward expansion of the warm Angola Current. Consequently, the simulated intertropical convergence zone (ITCZ) remains in its observed position over the northern Guinea Coast.

Both REMO and ROM experiments were carried out over a domain slightly larger than the usual CORDEX Africa domain (see Fig. 1).

The evaluation simulations, i.e., the dynamical downscaling forced by ERA-Interim, span the period from 1980 to 2014, whereas the historical runs, i.e., forced using MPI-ESM-LR as a lateral boundary condition, cover the period 1950–2005. The ERA-Interim-forced simulation aids in understanding the models' behavior under conditions close to reality. Conversely,

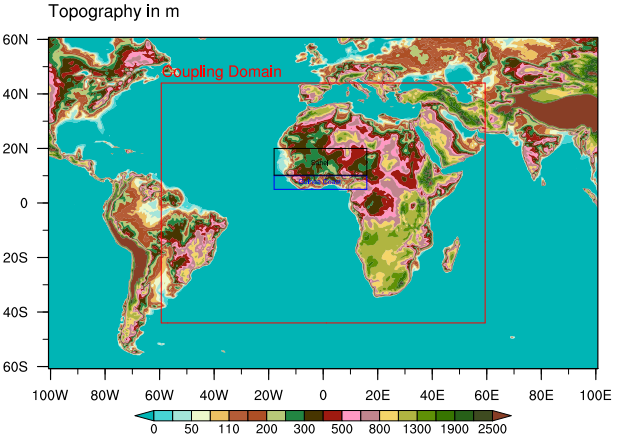

FIG. 1. The coupling area (red box) is displayed along with the topography of the domain (m) from NASA GTOPO30. Also shown are the Guinea Coast (blue box) and Sahel (black box), the combination of which forms the West African region.

TABLE 2. Description of reanalysis and satellite/gauge datasets employed for the intercomparison analysis.

Dataset	Institution	Horizontal resolution	Periods used	Reference
CRU TS4.05	Center for Atmospheric Research (NCAR) Climate Research Unit, University of East Anglia	0.5° × 0.5°	1980–2005	Harris et al. (2020)
GPCC v2020	Global Precipitation Climatology Centre	0.25° × 0.25°	1980–2005	Schneider et al. (2022)
CHIRPS2	Climate Hazards Group Infrared Precipitation with Stations	0.05° × 0.05°	1981–2005	Funk et al. (2015)
ERA5	ECMWF	0.25° × 0.25°	1980–2005	Hersbach et al. (2020)
MERRA-2	The Modern-Era Retrospective Analysis for Research and Applications, version 2	0.5° × 0.66°	1980–2005	NASA (2016)

the selection of MPI-ESM-LR for the historical simulation is driven by the need to avoid biases due to inconsistencies. Indeed, both MPI-ESM-LR and ROM share the same ocean component, and both REMO and ROM utilize identical physical parameterizations and a dynamical core, as ECHAM (the atmospheric component of MPI-ESM-LR; Jacob et al. 2012). This minimizes inconsistencies between the forcing and downscaling models. Simulations were done at 0.22° × 0.22°, i.e., ~25-km horizontal resolution, and the timeframe used for analyses is 1980–2005, based on the availability of reference datasets. However, the configuration of the oceanic component MPIOM is slightly different. As Cabos et al. (2020) described, it consists of a horizontal resolution reaching 10 km (eddy permitting) in the vicinity of the Iberian Peninsula. It gradually reduces up to 100 km in the southern seas. Hereafter, the terms REMO-ERA and REMO-MPI (ROM-ERA and ROM-MPI) will be used when referring to the uncoupled (coupled) simulations.

The experimental datasets are compared against three gauge-based, satellite-derived, or combined datasets, along with two gridded atmospheric reanalysis products (see Table 2 for full details). Notably, assessing climate models over equatorial Africa is very challenging because of the scarcity of ground-based measurements (Nicholson et al. 2019). The utilization of multiple reference datasets is the most often used solution to account for observational uncertainties. Given that reanalysis products are obtained from the assimilation of scattered ground-based measurements, we do not expect them to reproduce the exact observed climate, especially for precipitation, as also demonstrated by Gbode et al. (2023) for WA. However, because winds, specific humidity, and geopotential heights are constrained by observations, the water cycle produced is more accurate than from climate models. From this perspective, reanalysis data are used in this study qualitatively rather than quantitatively (i.e., as guidance). In other words, the reanalysis will enable us to ensure that the simulations realistically represent the baseline structure of the WAM system.

b. Methods

The study area is WA (18°W–16°E; 5°–20°N), which consists of two main regions: the humid Guinea Coast (18°W–16°E, 5°–10°N; indicated by the blue box in Fig. 1) and the transitional Sahel climate region (18°W–16°E, 10°–20°N; indicated by the black box in Fig. 1). The Guinea Coast experiences two rainfall maxima in June and September and a drier period in August (as known as "the little dry season") during which monthly rainfall weakens (<3 mm day^{-1}). In the Sahel region, the rainfall regime is unimodal, with precipitation peaking in August (>6 mm day^{-1}). As a result, we therefore focus our analyses on the July–August–September (JAS) season. This period corresponds to the peak of the WAM rainfall, as highlighted by Nicholson (2013), and corresponds to the maturation of physical processes and mechanisms that drive the WAM rainfall.

We assess how REMO and ROM improve the simulation of climatological WAM rainfall using the added value (AV) statistical metric, as defined by Dosio et al. (2015) and quantified using the following equation:

$$\mathrm{AV} = \frac{(X_{\mathrm{REMO}} - X_{\mathrm{ref}})^2 - (X_{\mathrm{ROM}} - X_{\mathrm{ref}})^2}{\mathrm{Max}[(X_{\mathrm{REMO}} - X_{\mathrm{ref}})^2, (X_{\mathrm{ROM}} - X_{\mathrm{ref}})^2]}, \quad (1)$$

where X represents the climatological spatial distribution of precipitation for the considered experiment (XREMO or XROM) or reference dataset X_{ref}. Following Dosio et al. (2015), the values of the AV are normalized by their maximum (Max) so that $-1 \leq \mathrm{AV} \leq 1$. AV directly compares REMO and ROM such that a positive AV indicates that the ROM coupled simulation improves over the REMO uncoupled simulation. Conversely, a negative AV indicates that the coupling does not lead to an improvement in the representation of the climate system. We have arbitrarily selected the threshold of 10^{-3}, i.e., the nearest thousandth ($-10^{-3} < \mathrm{AV} < +10^{-3}$), to highlight areas where the coupled model ROM exhibits equal performance to the uncoupled model REMO. The mean precipitation bias and the precipitation bias' statistical significance at 95% level through the two-tailed Student's t test are assessed. This helps to understand whether the improvement or deterioration is associated with an overestimation or underestimation of simulated rainfall.

To understand the reasons behind the sign of AV for each model group, we examined and compared REMO and ROM results in terms of their ability to reproduce the fundamental processes underlying the WAM system. One key distinction between the atmosphere-only and coupled ocean–atmosphere climate models is that the former respond to prescribed SSTs from the forcing ESMs, while the latter benefit from the more physical representation of heat and mass fluxes provided by interactive SSTs. Models with prescribed SSTs are not energetically closed at the surface, while coupled models are. Therefore, we examined how both groups of simulations represent regional features associated with the WAM, specifically

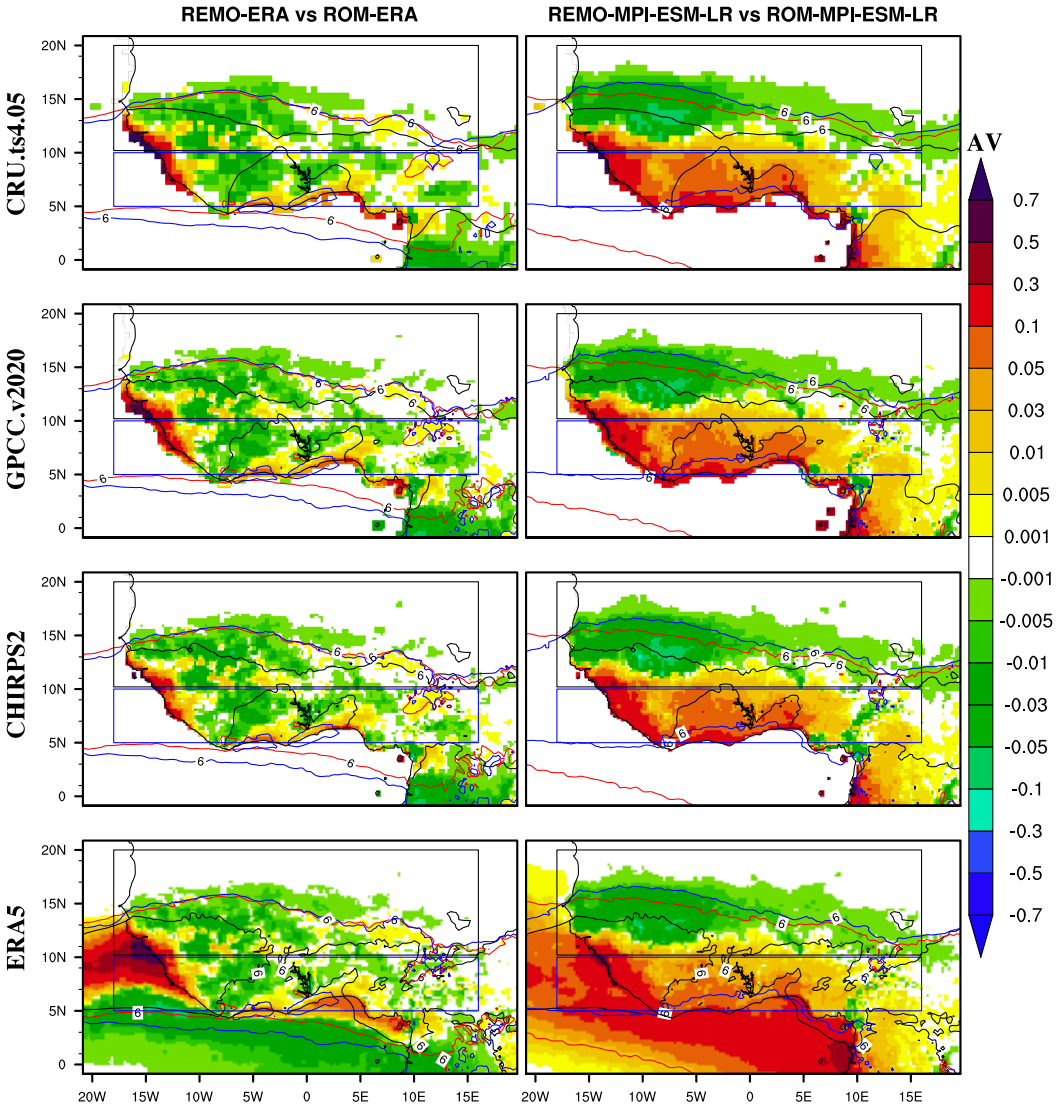

FIG. 2. AV of mean JAS WA precipitation in ROM experiments compared to REMO experiments. The reference datasets used are the observations CRU TS4.05, GPCC v2020, and CHIRPS2 and the reanalysis ERA5, over the period 1980–2005, except CHIRPS2 that covers the period 1981–2005. Positive (negative) values indicate a lower (higher) precipitation bias of ROM compared to REMO. Contours indicate the position of the rainband (i.e., precipitation larger than 6 mm day^{-1}) from the reference dataset (black), REMO (red), and ROM (blue). The blue box denotes the Guinea Coast (5°–10°N, 18°W–16°E), while the black box denotes the Sahel (10°–20°N, 18°W–16°E).

the marine ITCZ and continental monsoon rainband (d'Orgeval 2008), the mean seasonal positioning of the Sahara heat low (SHL; Lavaysse et al. 2009, 2010), the dynamics and intensity of the monsoon flows triggered by the land–sea thermal and pressure contrasts and which drive land–sea interactions (Fontaine et al. 1999; Parker et al. 2005); the West African westerly jet (WAWJ; Pu and Cook 2010, 2012), the midtropospheric African easterly jet (AEJ; Cook 1999; Nicholson and Grist 2003; Thorncroft et al. 2003), the upper-tropospheric tropical easterly jet (TEJ; Nicholson and Klotter 2020), and the atmospheric instability/stability associated with the convection (Fontaine et al. 1999). Done this way, an experiment brings plausible AV when the improvement occurs for the right reasons, meaning if the positive AV values are effectively accompanied by an improved representation of the underlying drivers that underpin the monsoon system (Tamoffo et al. 2020).

3. REMO versus ROM: The AV

The performance-based assessment of ROM against REMO in adding value to the mean JAS rainfall climatology is shown in Fig. 2. The reliability of these findings relies on the consistency observed across multiple reference datasets, including

CRU Time-Series version 4.05 (CRU TS4.05), GPCC v2020, and Climate Hazards Group Infrared Precipitation with Station data, version 2 (CHIRPS2), observations and the ERA5 reanalysis.

The choice of ERA5 is first motivated by its ability to reliably mimic the WAM rainfall seasonality, with the variability within the range of observational uncertainties (Quagraine et al. 2020; Gbode et al. 2023). Second, ERA5 features high horizontal and vertical resolutions among reanalyses available over equatorial Africa, crucial for capturing synoptic-scale mechanisms. Additionally, ERA5 is produced at an hourly time scale, essential for accounting for transient processes (Hersbach et al. 2020). We omitted MERRA-2 ($0.5° \times 0.66°$) from this analysis to prevent misinterpretation arising from interpolation errors. Notably, the alignment of results from ERA5 with those of three observations is of significance (Fig. 2). This consistency is particularly crucial as ERA5 will be used in subsequent analyses as a reference dataset to diagnose the physical mechanisms underlying the WAM system. The uncertainties related to the extent of improvement, deterioration, and neutrality are also indicated, using the standard deviation of the percentage values obtained from the four reference datasets.

Under the reanalysis-forced mode, where simulations are driven by the ERA-Interim reanalysis, the spatial pattern of AV includes a degradation ($AV < -0.001$) of the simulated precipitation over nearly half of the Guinea Coast (around 47.5% ± 2.5% of the area; see Fig. 2 and Fig. S1a in the online supplemental material) and a substantial portion of the southwestern Sahel (around 30% ± 1.30% of the Sahel; see Fig. 2 left column and Fig. S1b). There are improvements ($AV > +0.001$) in a small portion of the coastal areas of southwestern WA, extending toward the ocean (Fig. 2), and over localized sparse areas (with combined percentage area reaching 33% ± 2%). The results, based on the four reference datasets, are in agreement, showing improvements in approximately 10% ± 0.94% of the Sahel. However, toward the northern and in most parts of the eastern Sahel (around 60% ± 1.63% of the total area), REMO and ROM exhibit equivalent performance in simulating the mean seasonal precipitation climatology ($-0.001 \leq AV \leq 0.001$). Compared to the reference datasets, both the uncoupled REMO and coupled ROM models simulated higher precipitation along the Guinea Coast and over much of the Sahel, and REMO is drier than ROM everywhere (Fig. S2). Furthermore, it is notable that the simulated continental rainband appears to be too wide in both REMO and ROM simulations (Fig. 2).

When integrated under the ESM-forced mode, i.e., when the MPI-ESM-LR is used as the lateral boundary condition, the spatial pattern of AV features a dipole-like structure, consisting of positive AV (i.e., improvements) over almost all the Guinea Coast (around 88% ± 2.52%; Fig. 2 right column and Fig. S1a) and a small part of south-central and western Sahel (approximately 10% ± 2.75%; Fig. 2 and Fig. S1b), and negative AV (degradations) over almost half of the Sahel (46% ± 3%). Both REMO and ROM exhibit equivalent performance over 40% ± 3.41% of the Sahel. These models simulate higher precipitation amounts in most regions of the Guinea Coast and southern Sahel, relative to all reference datasets (Fig. S2). ROM-MPI decreases the wet bias over the Guinea Coast while strengthening the wet bias over the Sahel in comparison with REMO-MPI (Fig. S2). Furthermore, ROM improves the extent to the south of the southern side of the rainband, but there is no significant change along the northern side.

The descriptions above regarding how the southern and northern edges of the WAM rainband respond to coupling have drawn our attention to how the mean locations, not only of the WAM rainband but also of the marine ITCZ, are represented in the uncoupled and coupled experiments. The response of the marine ITCZ to coupling is also investigated because there is a link between the position and intensity of the ITCZ and precipitation in the Sahel. A shifted ITCZ further north induces more precipitation in the Sahel and vice versa, through a chain of processes described in Biasutti (2019) and references therein. Differences in the location of the ITCZ will provide information on how simulations of the large-scale drivers of the West African rainfall (e.g., Hwang et al. 2013; Song et al. 2018) are affected by the coupling.

To gain a general overview, we located the precipitation's barycenter, following d'Orgeval (2008). In fact, the WAM rainband is determined by computing the zonal mean (18°W–16°E) of the precipitation's barycenter, localized throughout latitudes 5°–20°N (Fig. 3a) using Eq. (2) as follows:

$$G(t) = \frac{\sum_{i=1}^{n} y_i P_i}{\sum_{i=1}^{n} P_i}, \tag{2}$$

where P_i is the precipitation at latitude y_i. The barycenter G is computed for each time step t. The intensity of the WAM rainband is defined as the precipitation rate at the barycenter's location (Fig. 3b). A similar exercise is employed to obtain the mean seasonal position of the ITCZ (Fig. 3c) and its intensity (Fig. 3b), but using the longitudinal band 60°W–60°E and latitudinal band 30°S–30°N, following Monerie et al. (2013). For consistency, precipitation is masked over the ocean specifically when calculating the WAM rainband positions and intensity. This was done since the three observations (CRU TS4.05, GPCC v2020, and CHIRPS2) lack data over the ocean.

The three observational datasets consistently show that the WAM rainband is centered around 10°N in July and reaches its northernmost position at around 10.5°N in August, before starting its southward retreat in September (Fig. 3a). The reanalysis-forced runs are the least effective in positioning the WAM rainband—they peak in September instead of August as in the MPI-ESM-LR-forced simulations and the observations. Similarly, the rainband intensity peaks in October in REMO-ERA and in September in ROM-ERA, instead of August (Fig. 3b). The ESM-forced runs outperform reanalysis-forced runs; however, they also misrepresent the latitudinal positioning of the rainband. Indeed, the uncoupled REMO-MPI experiment positions the WAM rainband too far south with

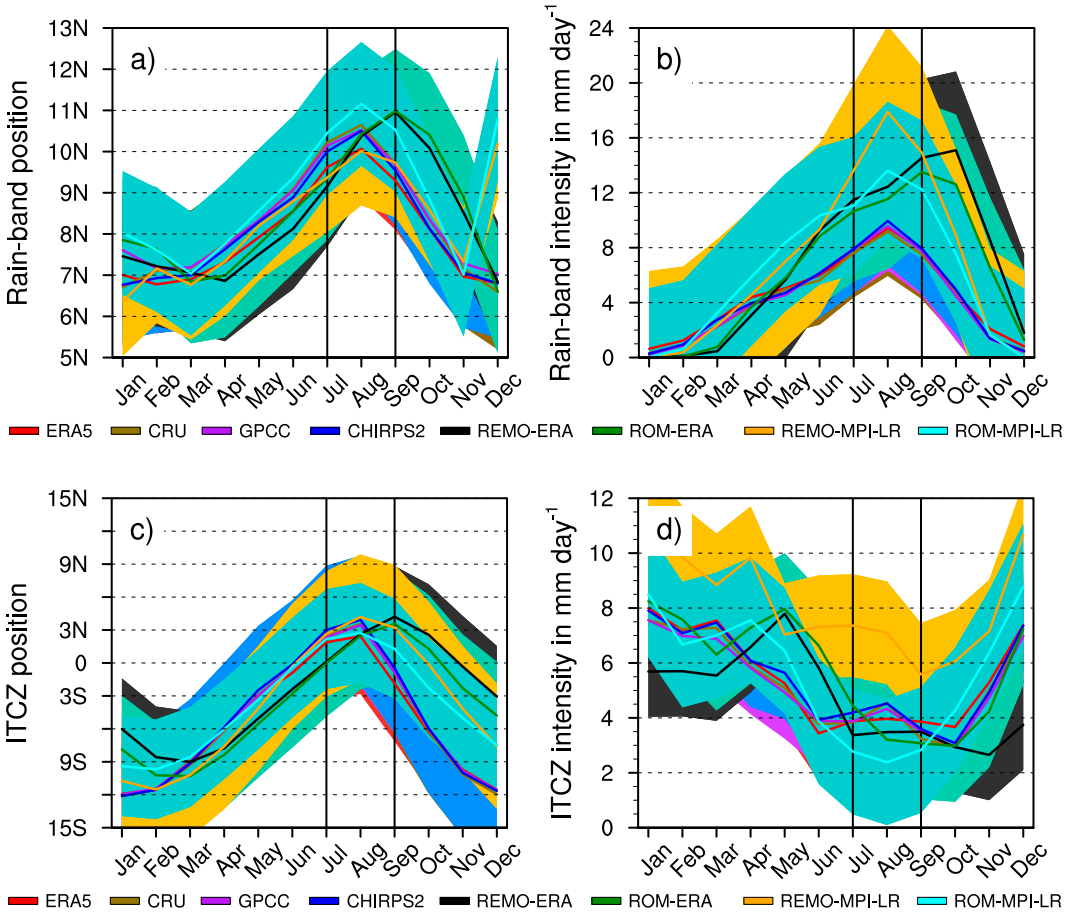

FIG. 3. The mean latitudinal location of the (a) WAM rainband and (c) ITCZ, defined as the barycenter of the zonal mean 18°W–16°E and 60°W–60°E, respectively, of the precipitation, localized over the latitudes 5°–20°N and 30°S–30°N, respectively, following d'Orgeval (2008); the mean intensity of the (b) WAM rainband and (d) ITCZ, defined as the rainfall amount recorded at the barycenter. The corresponding shaded area in color represents the standard deviation, indicating the variability in both the location in (a) and (c) and intensity in (b) and (d) of the rainband and ITCZ, respectively. The black bars denote the JAS months.

respect to CRU TS4.05, GPCC v2020, and CHIRPS2, but in quasi-agreement with the ERA5 reanalysis. In contrast, the coupled ROM-MPI experiment places the WAM rainband too far north. Nevertheless, both REMO and ROM forced by MPI-ESM-LR fall within the standard deviation of the observations (Fig. 3a). Additionally, although they overestimate the intensity of the rainband (Fig. 3b), they nonetheless capture the timing of its occurrence. Notably, the coupled ROM-MPI run improves the WAM rainband intensity relative to the uncoupled REMO-MPI run. Similarly, the reanalysis-forced simulations also misplace the intraseasonal locations of the ITCZ (Fig. 3c). They place the northernmost position in September instead of August, although its position around 3°N is better represented. ESM-forced simulations manage to capture the timing of the intraseasonal migration of the ITCZ, with the coupled ROM-MPI experiment performing better than the uncoupled REMO-MPI experiment. In terms of intensity (Fig. 3d), the uncoupled REMO-MPI simulation is the least accurate, with the 3-month intensity completely outside the standard deviation of the observations. Its counterpart, the coupled ROM-MPI simulation, improves but still underestimates the intensity of the ITCZ, with the August value outside the standard deviation of the observations.

It is worth mentioning that ESM-driven simulations successfully replicate the spatial structure of the rainfall trend, exhibiting enhanced rainfall in the major part of the Sahel and reduced rainfall in most parts of the Guinea Coast (Fig. S3). This concurs with the spatial pattern of added value as simulated by the coupled model ROM-MPI. A meridional (north/south) dipole is associated with a northward shift of the monsoon, aligning with our understanding of the variability in WAM rainfall and with the observed recovery trend (Biasutti 2019). However, the absolute amplitude of the trend is overestimated. This suggests that the primary driver of the precipitation trend remains unaltered by the coupling effect. Consequently, this influential factor is not, or at least not predominantly, linked to SSTs over the eastern equatorial Atlantic. Moreover, trends in precipitation, such as the drying observed

during the 1970s–80s followed by subsequent recovery, are also associated with external forcings such as greenhouse gases and anthropogenic aerosols (Monerie et al. 2022). It is worth noting that improvements in SSTs were not uniform across all oceanic basins. Furthermore, the coupling was implemented regionally rather than globally, indicating that outside the coupling domain (see Fig. 1), the SST is influenced by the global (biased) forcing data. These observations align with previous studies that have implicated large-scale forcing factors in the occurrence of the 1970s and 1980s drought in the Sahel (e.g., Janicot et al. 1996).

The coupling proves to be more beneficial under ESM-forced conditions, i.e., when forced by MPI-ESM-LR, than under reanalysis-forced conditions, i.e., when driven by ERA-Interim, particularly over the Guinea Coast. This result is consistent with the expected finding that under reanalysis-forced conditions, the coupling is not subject to the influence of biased boundary conditions. Instead, the atmospheric component REMO, which inherits SSTs derived from observations over the ocean, is influenced by the ERA-Interim reanalysis and not by the oceanic component MPIOM. Coupling under these conditions has biased the simulated atmospheric fields, although it has the potential advantage of better physically representing the heat and mass fluxes due to an interactive SST. ROM deteriorates the precipitation climatology in almost half of the Sahel, although it improves the positioning and intensity of the ITCZ during most of the monsoon time. The enhancement in the ITCZ representation suggests a better depiction of fine-scale air–sea interactions at higher atmospheric and oceanic resolutions in ROM, leading to a simulated ITCZ that is not shifted southward (Paxian et al. 2016). This leads to the hypothesis that the negative AV in the Sahel is associated with some local or regional WAM features that are either deteriorated or not improved by ROM. The next section addresses this issue.

4. The reasons behind AV

This section delves into the factors influencing the sign of AV. Our analysis centers on two key aspects: First, we explore how ROM simulates the WAM's drivers compared to REMO, aiming to clarify the plausibility of the AV results; and second, we investigate the sensitivity of the WAM's drivers to air–sea interactions. This secondary aspect enhances our comprehension of the mechanisms underlying the WAM, a knowledge valuable for both forecasting and projection purposes.

a. The SST response to coupling

SSTs affect atmospheric moisture content, which can be advected and result in changes in precipitation over land (Cook and Vizy 2006). In addition, SST gradients are associated with moisture convergence and ITCZ location, global energy budgets, pressure gradients, and monsoonal circulations (Cook 1999; Rodríguez-Fonseca et al. 2015). These processes are discussed in section 4c. Consequently, in Fig. 4, we depict the response of SSTs over the eastern Atlantic Ocean to coupling by computing the SST biases, i.e., the difference between the mean SST climatology of the simulations and that of ERA5 reanalysis. We focus on SSTs when first describing Fig. 4 because the coupling was performed over the oceans. Thus, land surface temperatures respond to the coupling over oceans, aiding in the understanding of surface temperature gradients subsequently analyzed in the next section.

ERA (ERA-Interim reanalysis) exhibits the weakest warm SST bias (+0.69°C) over the entire southern Atlantic Ocean, including the South Atlantic high pressure system. MPI-ESM-LR shows the highest positive SST bias (+2.19°C) over the entire Gulf of Guinea and Benguela–Angola coastal seas. These positive biases cover a large area extending southward along coastal areas and even over the South Atlantic high region. Figure S4 reveals that the coupling degrades SSTs in the reanalysis-forced ROM-ERA run. This experiment warms SSTs (+2°C), yet ERA-Interim previously exhibited a weaker SST bias value (+0.69°C). In contrast, ROM improves SSTs over the eastern Atlantic Ocean compared to MPI-ESM-LR (Fig. S4). Specifically, ROM-MPI reduces the magnitude of warm SST bias (+0.54°C) that previously featured MPI-ESM-LR (+2.19°C). Generally, the driving MPI-ESM-LR appears warmer in most parts of the Atlantic Ocean compared to ROM-MPI-ESM-LR. As a likely response, ROM-MPI-ESM-LR experiences higher sea level pressure (not shown) in most regions of the ocean than REMO-MPI-ESM-LR.

Figure S5 shows that the cooler SSTs simulated by ROM-MPI compared with REMO-MPI lead to a decrease in evaporation over the eastern Atlantic Ocean. The weakening in the evaporation is larger in coastal areas (north of the equator) with a change in the bias sign. Inland and compared to REMO-MPI, ROM-MPI decreases evaporation over the Guinea Coast, but enhances evaporation over the Sahel. The strengthening of evaporation over the Sahel aligns with the previously noted bolstered precipitation (Tamoffo et al. 2023b). On the other hand, the increase in evaporation over the Sahel suggests the influence of coupling on the radiative budget (Vizy et al. 2013), with feedback on regional WAM features such as the SHL. This point is further explored in section 4e. At first glance, changes in SSTs are associated with modifications in air–sea interactions, including the land–ocean thermal contrast and the resulting pressure contrast that determine the force of monsoon fluxes. This aspect is examined in the following section.

b. Air–sea interactions' response to coupling

Figure S2 demonstrates that under the reanalysis-forced mode driven by ERA-Interim reanalysis, there are no significant differences between REMO and ROM in terms of precipitation magnitude across WA, with REMO only slightly drier than ROM. However, the ESM-forced experiments, i.e., when driven by MPI-ESM-LR, showed that REMO is moister than ROM along the Guinea Coast but drier than ROM in the Sahel region. We hypothesize that depending on the forcing mode, changes in air–sea interactions resulting from coupling could be responsible for the spatial pattern of moistening or drying in each experiment. Surface thermal and pressure gradients or contrasts act as drivers for these land–sea interactions (Zhao et al. 2005). To test our hypothesis, we diagnosed the representativeness of these factors in each simulation. Figure 5 compares REMO and ROM against the

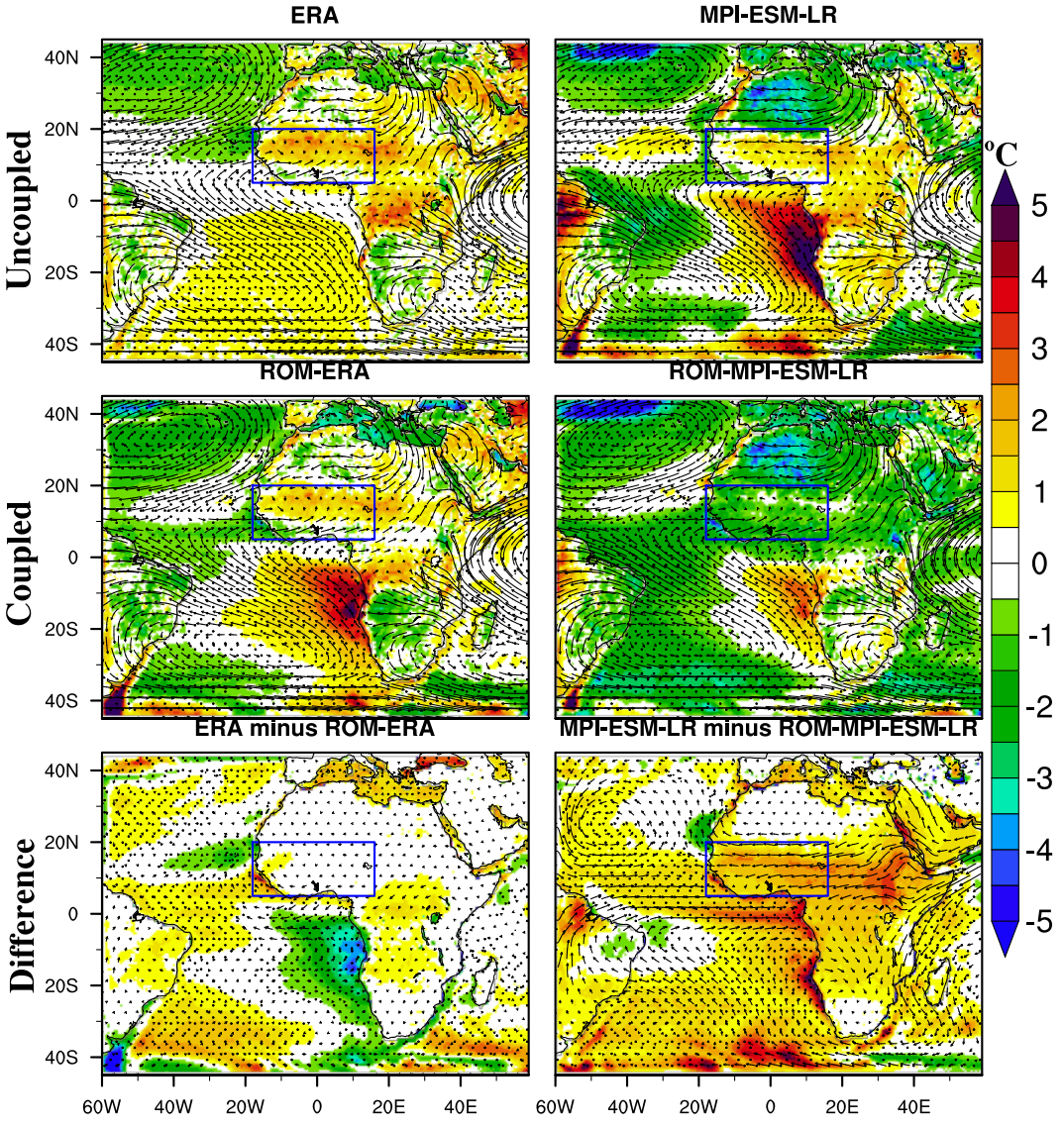

FIG. 4. Mean (1980–2005) JAS SST biases (shaded) computed relative to the ERA5 reanalysis and the mean JAS circulation at 850 hPa. Also shown are the differences between the ERA and MPI-ESM-LR experiments and their corresponding ROM-downscaled experiments. For the four top (two bottom) panels, the stipples occur where the difference between the dataset under consideration and the ERA5 reanalysis dataset (the difference between ERA/MPI-ESM-LR and ROM) is statistically significant at the 95% confidence level after the Student's *t* test is applied. The blue boxes indicate the WA region.

reanalysis datasets (Fig. 5a) and, subsequently, intercompares REMO and ROM in each forcing mode by illustrating the difference (REMO minus ROM) in the meridional temperature gradient at 925 hPa (Fig. 5b). Our hypothesis is well founded. Indeed, over the ocean and outside the latitude band of 20°–10°S and south of 38°S, REMO-ERA features a weaker meridional temperature gradient elsewhere across the ocean basin compared to ROM-ERA (Fig. 5b). A direct consequence is the reduced amount of captured moisture over the ocean per unit of time and its transport toward the Guinea Gulf due to weaker winds. This results in a drier Guinea Gulf in REMO-ERA compared to ROM-ERA (Fig. S2).

Inland, although REMO-ERA exhibits a positive and stronger surface temperature gradient along the Guinea Coast (0°–10°N) compared to ROM-ERA, this difference is nearly canceled out over the Sahel region (10°–20°N) with ROM-ERA's gradient slightly stronger than that of REMO-ERA. Lower moisture availability in the Guinea Gulf in REMO-ERA relative to ROM-ERA leads to weaker inland moisture penetration in REMO-ERA than in ROM-ERA, conducive to a drier REMO-ERA over central and eastern Sahel. The positive thermal gradient over the Guinea Coast is a favorable condition for moisture depletion in the region. A similar process may also be at play with the WAWJ, reducing precipitation in the western

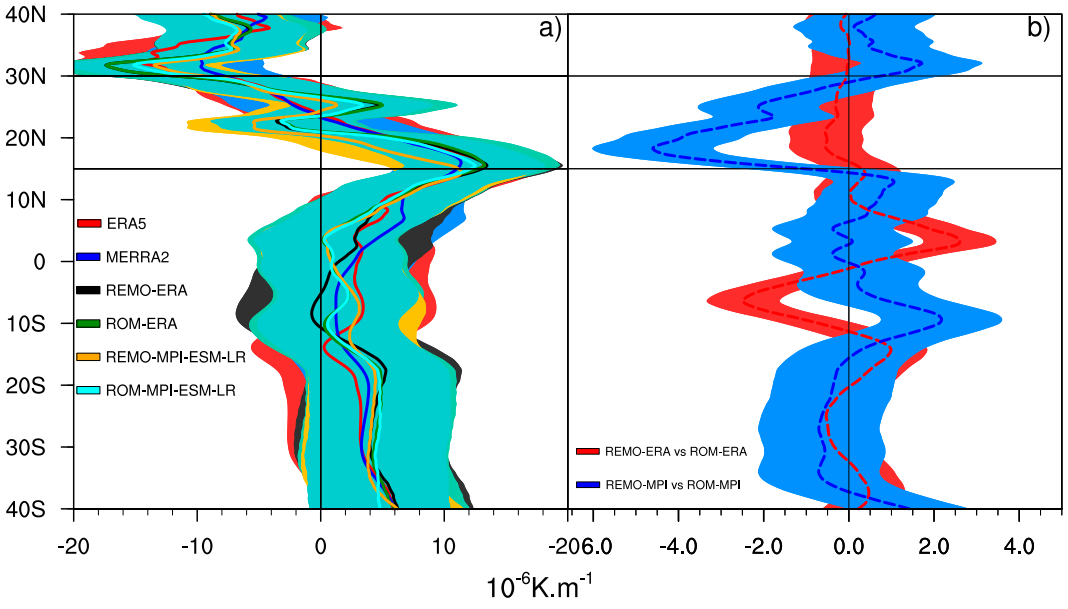

FIG. 5. JAS climatology (1980–2005) of (a) the latitudinal migration of the 925-hPa temperature gradient and (b) difference ($\times 10^{-6}$ K m^{-1}) averaged over the longitudes 10°W–10°E, from ERA5, MERRA-2, REMO/ROM-ERA, and REMO/ROM-MPI. The horizontal black bars delimit the latitudinal band 15°–30°N, and the vertical bar is the gradient value 0. The corresponding shaded area in color represents the standard deviation, indicating the variability in the temperature gradient.

Sahel. REMO-MPI shows a weaker meridional thermal gradient than ROM-MPI from the south up to 15°S and then a stronger gradient almost elsewhere in the ocean basin (Fig. 5b). Over the continent, REMO-MPI simulates a softly stronger surface temperature gradient than ROM-MPI along the Guinea Coast, which intensifies south of the Sahel (10°–15°N). In contrast, north of 15°N, the gradient reverses and becomes stronger in ROM-MPI from the northern Sahel toward the Sahara (up to 30°N; Fig. 5b). The stronger thermal gradient in ROM-MPI over the northern Sahel may have contributed to increased moisture influx into the interior of the Sahel.

Figure 6 summarizes the changes in land–sea contrasts, including the thermal contrast ΔT (Fig. 6a) and the pressure contrast ΔP (Fig. 6b). The terms ΔT and ΔP are calculated as the differences between land surface temperature and ocean SST, and land surface pressure and sea level pressure, respectively, between the Sahara continental mass (15°W–16°E; 20°–30°N) and the eastern South Atlantic Ocean (15°W–16°E; 0°–20°S). The (ΔT, ΔP) couple adequately reflects the difference in rainfall between REMO and ROM. In fact, REMO-ERA and ROM-ERA, which simulated similar rainfall amounts, also exhibit nearly identical ΔT and ΔP distributions. Additionally, both reanalysis-forced experiments place the peak of ΔP in August instead of July, as in the coupled cases, consistent with the 1-month delay in the occurrence of precipitation peak (Fig. 3). Conversely, REMO-MPI, which simulates a drier Sahel compared to ROM-MPI, also simulates weaker temperature and pressure gradients than ROM-MPI. These results suggest that the difference in the amount of advected moisture inland is responsible for the spatial patterns of simulated rainfall in REMO and ROM. The differences in these gradients lead to variations in the strength of the atmospheric circulation and monsoonal flows and their penetration depth inland. These assumptions are discussed in the following section.

c. *Low-level circulation response to coupling*

Figure 7 shows the low-level circulation associated with the WAM rainfall climatology in JAS. REMO-ERA and ROM-ERA, which exhibit quasi-similar WAM rainfall patterns, also display similar low-level moisture transport (Fig. S6). The slightly drier nature of REMO-ERA relative to ROM-ERA is strongly associated with their respective regional moisture convergence in WA and corroborates the assumptions formulated in section 4b. Indeed, as shown in Fig. 7, REMO-ERA simulates lower monsoon flows (42.67 kg m^{-1} s^{-1}) than ROM-ERA (47.51 kg m^{-1} s^{-1}) and weaker moisture emanating from the WAWJ (41.01 kg m^{-1} s^{-1}) than ROM-ERA (46.22 kg m^{-1} s^{-1}). Thus, ROM-ERA degrades the representativeness of monsoon fluxes, in association with the deterioration in SSTs over the eastern equatorial Atlantic Ocean (Fig. S4) and the deterioration in accuracy in simulating the land–sea thermal and pressure contrasts (Fig. 6). This has to be compared to a lower monsoon flow (35.79 kg m^{-1} s^{-1}) and WAWJ (22.17 kg m^{-1} s^{-1}) in ERA5 than in ROM-ERA and REMO-ERA. ROM-MPI better simulates the SSTs of the eastern tropical Atlantic Ocean than REMO-MPI (Fig. 4), resulting in an improved simulation of monsoon fluxes (39.91 kg m^{-1} s^{-1}) compared to ERA5 (35.79 kg m^{-1} s^{-1}) and MERRA-2 (39.53 kg m^{-1} s^{-1}) reanalyses and relative to REMO-MPI (57.93 kg m^{-1} s^{-1}). However, the simulated transient fluxes through the northern boundary of the Guinea Coast toward the Sahel (51.95 kg m^{-1} s^{-1}) as well as moisture

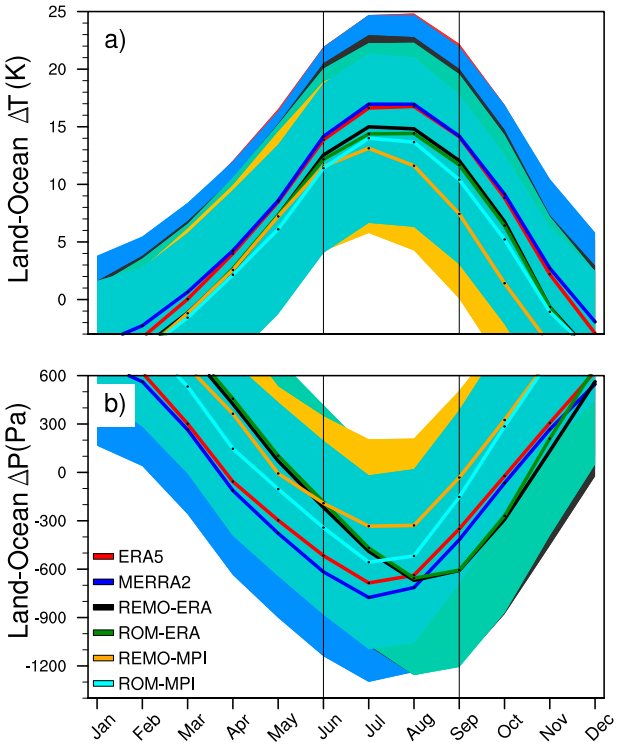

FIG. 6. Mean (1980–2005) seasonality of the near-surface (a) land–ocean temperature difference [thermal contrast ΔT (K)] and (b) land surface pressure and ocean sea level pressure difference ΔP (Pa) between the interior of the continent (15°W–16°E, 20°–30°N) and the southeastern Atlantic Ocean (15°W–16°E, 0°–20°S), for the reanalyses ERA5 and MERRA-2 and for REMO and ROM experiments. The corresponding shaded area in color represents the standard deviation, indicating the variability in (a) ΔT and (b) ΔP, respectively.

supplied from the WAWJ (40.23 kg m^{-1} s^{-1}) are degraded by the coupled ROM-MPI model compared to its atmosphere-only counterpart, REMO-MPI (37.83 and 22.85 kg m^{-1} s^{-1}, respectively), which is closer to the ERA5 and MERRA-2 reanalyses (30.35 and 35.81, and 22.17 and 23.15 kg m^{-1} s^{-1}, respectively).

We put forward two hypotheses based on the aforementioned results: 1) Equatorial east Atlantic Ocean SSTs influence the rainfall system through direct teleconnections over the Guinea Coast, but indirectly in the Sahel, and the SST–Sahel rainfall relationships are not improved by coupling. This may explain why, under ESM-forced conditions, positive AV in the equatorial east Atlantic Ocean SSTs leads to positive precipitation AV along the Guinea Coast but negative in the Sahel. 2) The modulating effect of SSTs on the Sahel rainfall system is of secondary importance to local/regional forcing factors which are deteriorated by coupling. However, some of these local/regional factors, in return, respond to large-scale and even extratropical forcing factors. The accuracy of these factors could be either improved or degraded by coupling. Numerous studies have already demonstrated the modulating role of SSTs on Sahel rainfall (e.g., Zhao et al. 2005; Cook and Vizy 2006; Giannini et al. 2013; Rodríguez-Fonseca et al. 2015). For instance, Vizy and Cook (2002) showed that anomalously high SSTs in the Guinea Gulf lead to reduced rainfall in the Sahel but, conversely, increased rainfall along the Guinea Coast. This previous study is consistent with ours because, as found in sections 3 and 4a, the coupled ROM-MPI run attenuates the warm SST bias in the Guinea Gulf as simulated by the uncoupled REMO-MPI run, which correlates with the drier behavior of ROM-MPI along the Guinea Coast but wetter in the Sahel (Fig. S2). This suggests that the second hypothesis is more likely. As seen in Fig. 7, we posit that stronger moisture fluxes from the WAWJ and northward advection crossing the northern border of the Guinea Coast are responsible for the increased precipitation in the Sahel simulated by the ROM-MPI coupled experiment. Consistently, Pu and Cook (2012) demonstrated that wet periods in the Sahel feature enhanced westerly moisture advection originating from a strengthened WAWJ. This leads to increased moisture availability in the Sahel's lower layer, thereby reducing atmospheric stability. The strengthening of inward flows in the Sahel through the northern border of the Guinea Coast is linked to an enhanced surface temperature gradient between 15° and 30°N. In the next section, we examine whether the responses of other local/regional factors of the WAM system to coupling are associated with the pattern of rainfall.

d. AEJ and TEJ responses to coupling

Two of the primary features of the WAM system are the AEJ and TEJ (Sultan and Janicot 2003; Nicholson 2013). The AEJ is the midtropospheric (700–600 hPa) response of the more local and mesoscale features of the WAM system. While the AEJ is generated by an increasing/decreasing meridional thermal/soil moisture gradient from the moistened Guinea Gulf to the hot Sahara (Nicholson and Grist 2003; Cook 1999), it is primarily sustained by surface heating, which generates dry convection in the Sahara thermal low region (Cook 1999; Thorncroft and Blackburn 1999; Chen 2005). The passage of the AEJ is also associated with disturbances known as African easterly waves (AEWs) with a periodicity ranging from 2 to 10 days and wavelengths ranging from 2 to 4×10^3 km, which develop through mixed baroclinic–barotropic instability along the AEJ (Kiladis et al. 2006; Thorncroft et al. 2008). While analyses based on AEWs are not conducted in this study due to the unavailability of daily simulation data, conclusions can still be drawn from the analyses conducted on the AEJ. Wet conditions in the Sahel are associated with a northward shift and weaker AEJ, conditions that favor increased moisture convergence into the Sahel and, subsequently, mesoscale convective systems feeding convection (Nicholson and Grist 2003). The TEJ owes its existence to the meridional thermal contrast between the Tibetan highlands and the Indian Ocean (Koteswaram 1958). Numerous previous studies argued that in the Sahel, wet years exhibit a strong TEJ, while dry years exhibit a weak TEJ, with a contrast that can reach a factor of 2 (Nicholson and Grist 2003; Lemburg et al. 2019). Nicholson and Klotter (2020) questioned the link between the TEJ and Sahel rainfall. They demonstrated that anomalously wet years

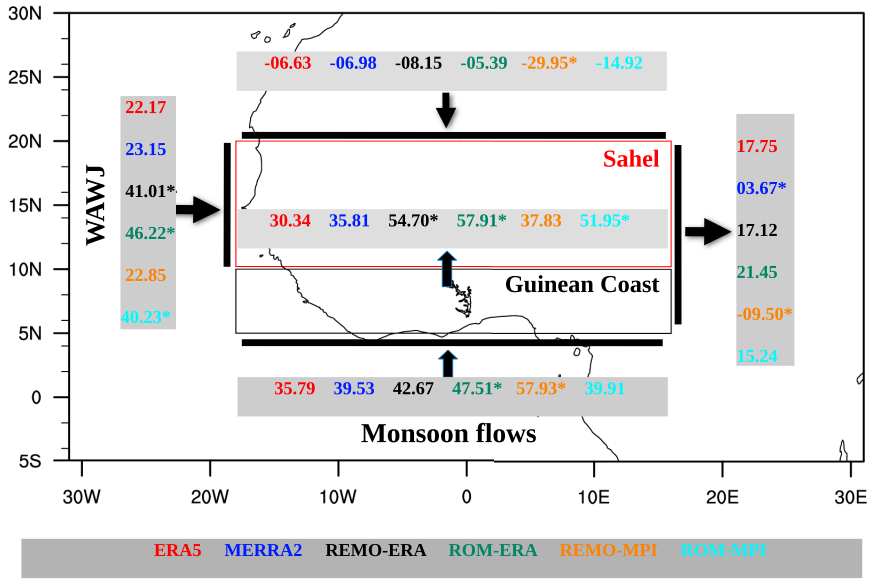

FIG. 7. Low-level atmospheric moisture transport (1000–850 hPa) into the WA interior across each boundary. The numbers indicate the mean seasonal amount (1980–2005) of water vapor (kg m^{-1} s^{-1}) crossing each boundary, based on reanalysis datasets and REMO and ROM experiments. Asterisks (*) indicate the significance of values at 95% according to the *t* test. The black box represents the Guinea Coast, and the red box represents the Sahel.

can occur without an anomalously strong TEJ. They argued that additional modeling studies are needed to determine whether Sahel rainfall and the TEJ respond to the same forcing factors and that extratropical circulations control the TEJ via global SSTs.

Figures 8a and 8b show that the coupled experiment ROM-MPI, which is moister over the Sahel than its counterpart uncoupled REMO-MPI experiment, also shifts the core of the AEJ northward. However, both experiments realistically represent the timing and latitudinal migration of the jet. The coupling also improves the intensity of the AEJ in July and September (Fig. 8c), in association with enhancement in the surface meridional temperature gradient (Fig. S7). Once again, there are no important differences between the two reanalysis-forced simulations, as they exhibit remarkably similar AEJ characteristics and surface thermal gradients during the monsoon time. Figure S8 reveals that the coupling considerably improves the AEJ and TEJ representations when simulations are forced with MPI-ESM-LR, although the mean seasonal intensity remains slightly underestimated. A notable increase in magnitude (Fig. S8 and Fig. 9c) and an anomalous northward displacement (Figs. 9a,b) of the TEJ are evident in the coupled ROM-MPI relative to REMO-MPI and are consistent with the enhanced precipitation over the Sahel. While the coupling affects the latitudinal–time positioning of the TEJ (Figs. 9a,b), it significantly improves its intensity (Fig. 9c) and spatial pattern (Fig. S9). There are also discrepancies in the longitudinal direction as simulated by the atmosphere-only experiment REMO-MPI, which are resolved in the coupled ROM-MPI simulation (Fig. S9). REMO-MPI strongly underestimates the TEJ over central equatorial Africa between 10° and 30°E, a feature that is improved in the coupled ROM-MPI run.

As AEWs are atmospheric disturbances related to the passage of the AEJ (Diedhiou et al. 1999; Thorncroft et al. 2008; Leroux and Hall 2009), improvement of the AEJ offers potential insights into the simulation of AEWs (Tamoffo et al. 2023a). In the present study, we did not investigate the reasons behind the disparities in the simulated TEJ. However, the latest study by Nicholson and Klotter (2020) sheds light on the drivers of TEJ, indicating that this component of the WAM system is influenced by large-scale forcing factors. Due to the limited area used in dynamical downscaling, accurately diagnosing these factors is challenging. Nevertheless, differences between REMO-MPI and ROM-MPI in simulating the TEJ stand out (Fig. S9), whereas differences are smaller for the AEJ (Fig. S8). This suggests that the coupling configuration employed in this study improves the TEJ's strength more than the AEJ's strength, especially in terms of intensity. This result aligns with the recent arguments made by Nicholson and Klotter (2020) that the TEJ is heavily influenced by extratropical factors, which act through global SSTs. The global nature of the oceanic component of ROM, MPIOM, contributes to enhancing the accuracy of SSTs in the ocean basins that drive the TEJ. However, it is important to note that the coupling has led to improvements in the intensity of both jets, leaving the debate solely on the too-northward shifting of their cores as opposed to reanalyses. A work by Whittleston et al. (2017) also emphasized the lack of a jet–rainfall relationship in climate models over the West African Sahel. Furthermore, as previously mentioned, the overall condition of the jets aligns with increased rainfall over the Sahel, resulting in

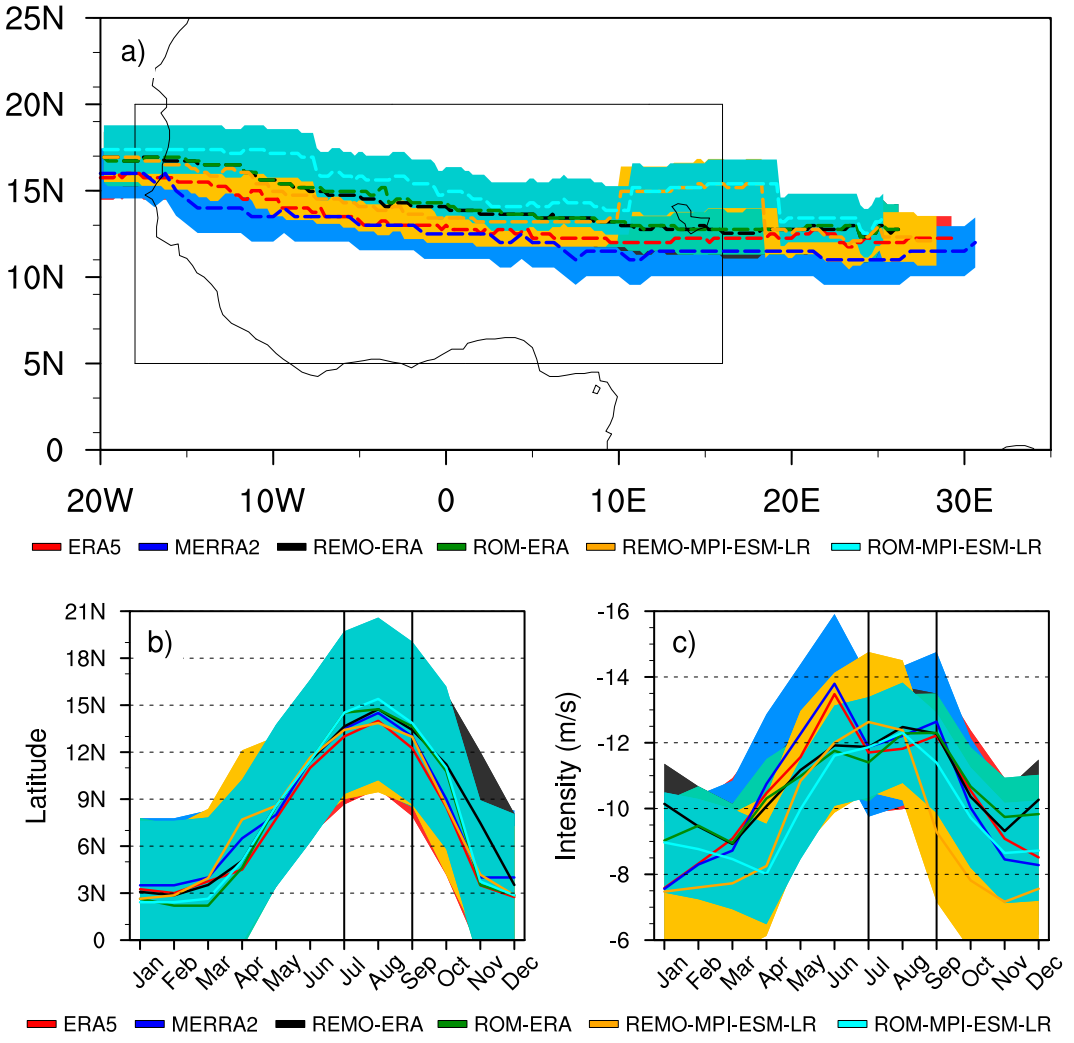

FIG. 8. Long-term mean (1980–2005) JAS (a) latitudinal–longitudinal location, (b) latitudinal–time location (°N), and (c) intensity (m s^{-1}) of the mean core of the AEJ (U wind ≤ -6 m s^{-1} at 700 hPa), from reanalysis data ERA5 and MERRA-2 and from REMO and ROM experiments. The corresponding shaded area in color represents the standard deviation, indicating the variability in both the AEJ location in (a) and (b) and intensity in (c). The black box denotes WA.

negative AV. The coupled ROM-MPI run indicates that the degraded or unimproved rainfall climatology over the Sahel can be primarily attributed to biases in regional or local WAM's forcing factors.

e. The SHL's response to coupling

Figure 10 allows assessing the assumptions from section 4c and demonstrates that the inadequate representation of the SHL is not associated with the negative AV over the Sahel. Instead, it points to the overestimated WAWJ and northward low-level cross-northern border Guinea Coast flows as potential contributing factors. Indeed, the SHL is detected through the 850-hPa temperature climatology (Lavaysse 2015) and the low-level atmospheric thickness (LLAT), i.e., the difference in geopotential heights between 700 and 925 hPa (Lavaysse et al. 2009). Both REMO-ERA and ROM-ERA exhibit similar biases in the SHL compared to ERA5, consistent with the similarities in their simulated rainfall patterns in the Sahel (Fig. S2). However, while the coupling in ROM-MPI brings significant improvements in the representation of SHL (previously strongly underestimated by REMO-MPI by ~4°C), the strength of the thermal depression remains lower than that simulated by ERA5 (~2°C). Thus, the ESM-forced simulations underestimate the magnitude of the SHL. A similar conclusion is reached using LLAT (Fig. 10).

Regarding the latitudinal displacement during the monsoon period (Fig. 11a), the two simulations driven by ERA-Interim remain pretty similar, while in the simulations driven by the ESM MPI-ESM-LR, the coupling improves the latitudinal positioning of the SHL, with ROM-MPI following the ERA5 curve closely. Here, the enhancement consisted of shifting the SHL's core further north, in line with the

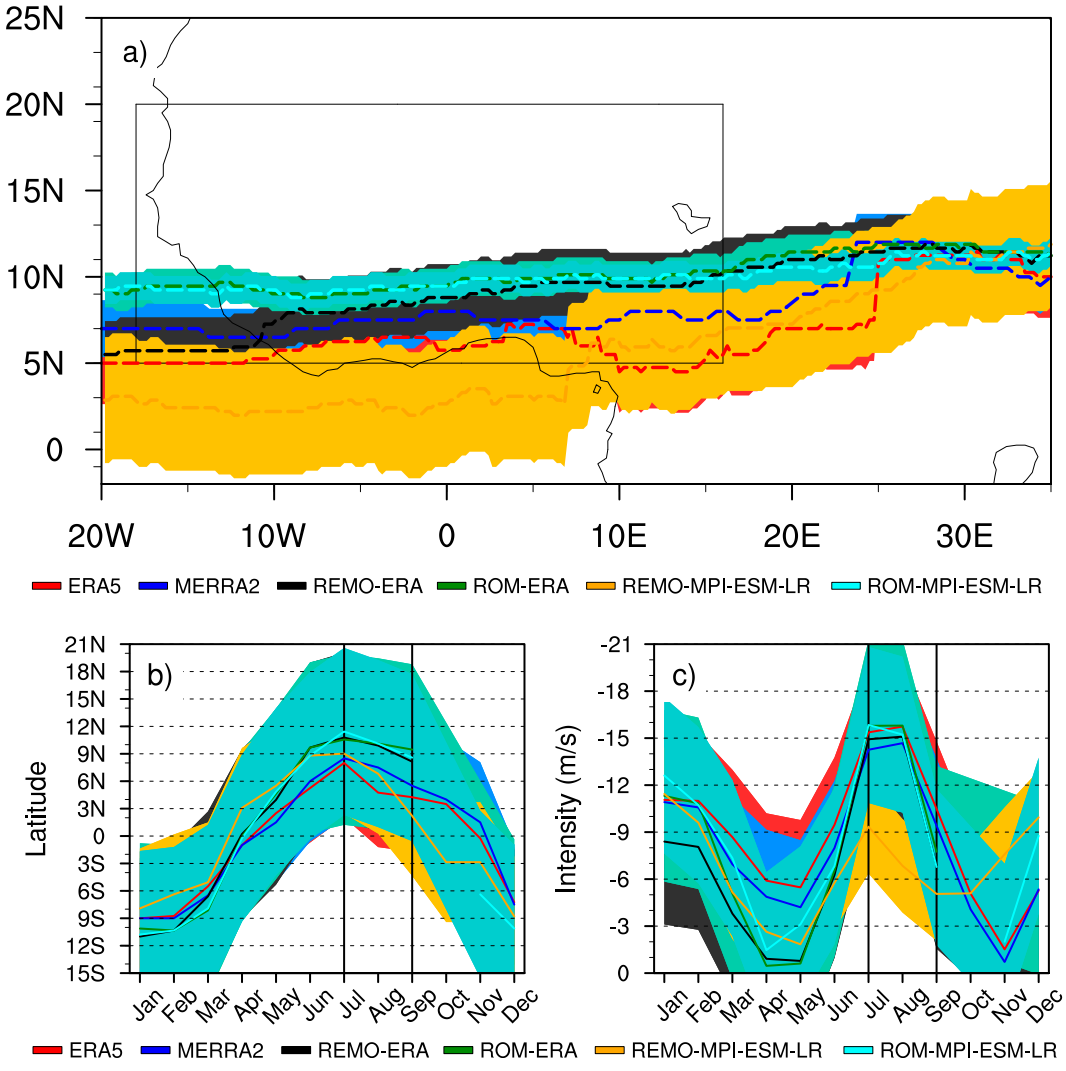

FIG. 9. Long-term mean (1980–2005) JAS (a) latitudinal–longitudinal location, (b) latitudinal–time location (°N), and (c) intensity (m s^{-1}) of the mean core of the TEJ (U wind ≤ -6 m s^{-1} around 200 hPa), from reanalysis data ERA5 and MERRA-2 and from REMO and ROM experiments. The corresponding shaded area in color represents the standard deviation, indicating the variability in both the TEJ location in (a) and (b) and intensity in (c). The black box denotes WA.

increased rainfall over the Sahel (Lavaysse et al. 2010; Dixon et al. 2017). Figure 11b shows that the reanalysis-forced runs simulate a stronger SHL than the ERA5 throughout the monsoon season. Contrastingly, REMO-MPI and ROM-MPI simulate a weaker SHL. Notably, ROM-MPI tends to improve REMO-MPI, especially in August and September, consistent with improvements in the AEJ during the same monsoon months (Fig. 8c).

Previous research supports the plausibility of the aforementioned findings. For instance, ROM-MPI models a stronger SHL than REMO-MPI, in accordance with its higher land–ocean thermal contrast ∇T compared to that of REMO-MPI (Biasutti et al. 2009). Despite the fact that the coupling enhances the SHL in association with improvements in the east equatorial Atlantic Ocean SSTs, its strength remains persistently underestimated. This result supports the earlier conclusion of Dixon et al. (2017), who reported that the modulating effects of SSTs on the features of the SHL's climatology are secondary to those of atmospheric biases. Several studies argued that the strength of the SHL is influenced by variability in the local radiative budget, which, in turn, is associated with large-scale processes (Vizy and Cook 2009; Chauvin et al. 2010; Lavaysse et al. 2010; Dixon et al. 2017). Indeed, the process generally involves cooling/warming of the Sahara and, consequently, the SHL region, through the advection of cold/warm air from midlatitude waves (Chauvin et al. 2010) or Mediterranean regions (Vizy and Cook 2009). The local radiative budget may also be modified by advected moist air over the SHL (Engelstaedter et al. 2015) and by dust transported by atmospheric circulation (Lavaysse et al. 2011; Schepanski et al. 2017).

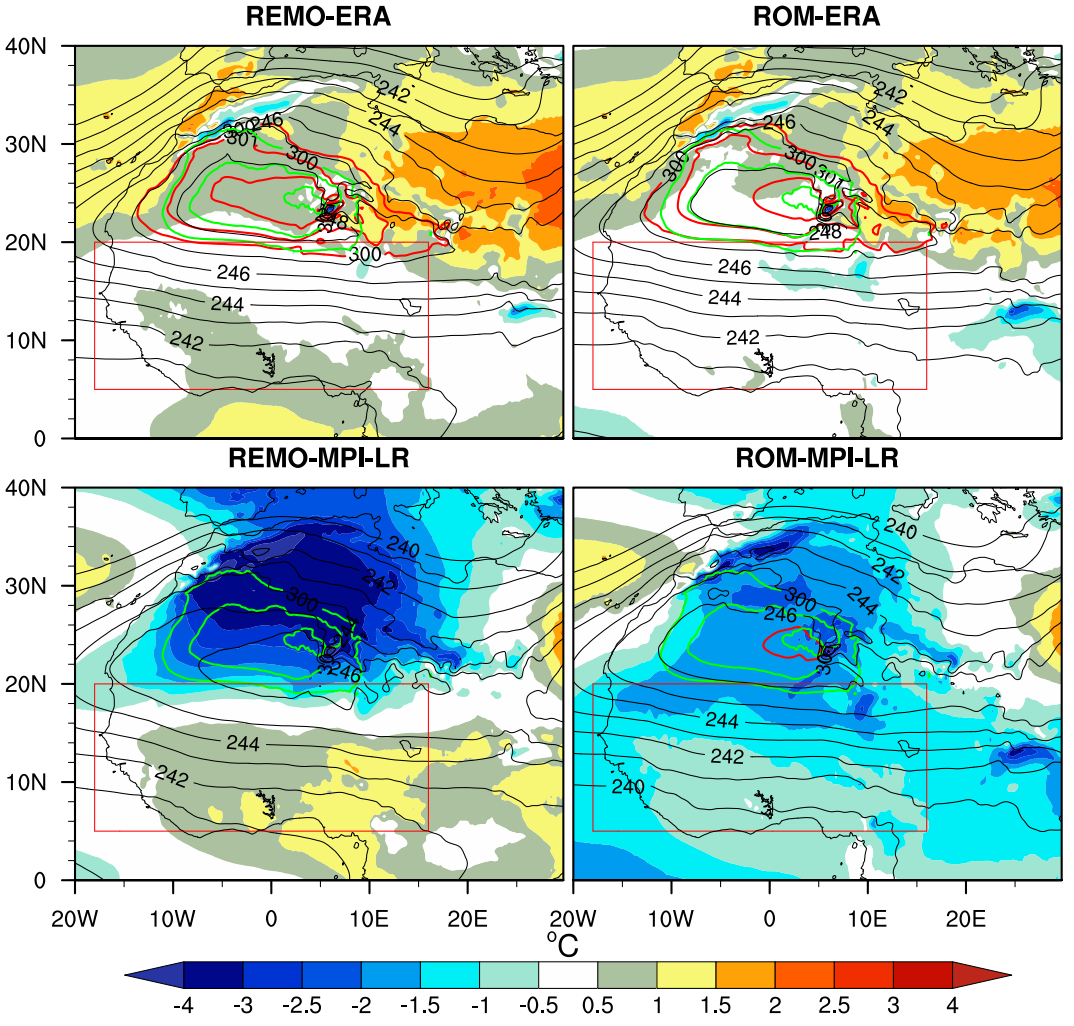

FIG. 10. Mean JAS seasonal SHL bias (REMO/ROM minus ERA5) highlighted by the mean JAS 850-hPa temperature (°C; shaded). The red contour line represents the heat low location in the analyzed dataset, while the green contour line represents the heat low location in ERA5 (used as a reference dataset), using ≥300-K temperature contours. Black contours are the LLAT (m), i.e., the difference in geopotential heights between 700 and 925 hPa (Lavaysse et al. 2009). The red boxes indicate the WA region.

Figure S10 illustrates that effectively biases in the radiative budget largely account for the biases in the strength of the SHL. Reanalysis-forced runs, which slightly overestimate the strength of the SHL, simulate slight negative biases (−10.55 and −9.23 W m^{-2}) in the net surface solar radiation (NSSR). Conversely, REMO-MPI and ROM-MPI, which underestimate the strength of the SHL, strongly underestimate the NSSR (−23.65 and −19.97 W m^{-2}, respectively). Furthermore, the difference between REMO-MPI and ROM-MPI (up to −3.68 W m^{-2}) reveals that the improvement provided by the coupled ROM-MPI model is associated with the enhancement in the NSSR, which has mitigated the magnitude of negative biases. The investigation into the reasons behind changes in the local radiative budget over the SHL's region is reserved for forthcoming research. The outstanding question is whether the climatology of simulated precipitation over the Guinea Coast and Sahel, in response to changes in moisture availability, is preceded by atmospheric instability/stability conditions associated with convection.

f. Atmospheric instability response to coupling

Ninety percent of precipitation over the Sahel originates from mesoscale convective systems (MCSs; Nesbitt et al. 2006), highlighting the crucial role of convection in modulating the region's rainfall pattern. Given this perspective, it is necessary to investigate how modifications in the atmospheric circulation, in response to the coupling, induce changes in atmospheric instability. We utilized the moist static energy (MSE) thermodynamic metric, which facilitates the connection between atmospheric circulation with regional or local moisture availability. Through the use of MSE, we examined the atmospheric instability or stability associated with the climatology of rainfall, as modeled by each experiment. The MSE is defined as shown in Eq. (3):

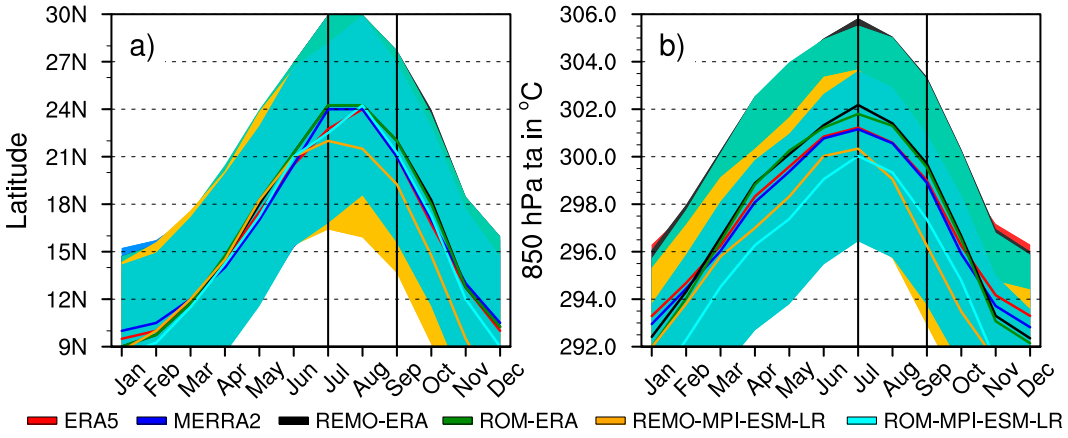

FIG. 11. (a) The mean latitudinal location of the heat low during the JAS months, defined as the point of the maximum zonal-mean (18°W–16°E) 850-hPa air temperature, localized over the latitudes 0°–35°N; (b) the mean intensity of the heat low, defined as the temperature recorded at the point of 850-hPa air temperature maximum. The corresponding shaded area in color represents the standard deviation, indicating the variability in both the heat low location in (a) and intensity in (b). The black bars denote the JAS months.

$$\mathrm{MSE} = c_p T + gz + Lq, \tag{3}$$

with the first two terms on the right-hand side representing the dry static energy (DSE; DSE = $c_pT + gz$) input; c_pT is the sensible heat; gz is the potential energy; Lq is the latent static energy (LSE; LSE = Lq); c_p is the specific heat at constant pressure; T is the air temperature; g is the gravitational constant; z is the geopotential height; L is the latent heat of condensation; and q is the specific humidity. To emphasize the difference in instability or stability between experiments, we estimate, for each run, the latitudinal average (between 5° and 10°N for the Guinea Coast and 10°–20°N for the Sahel) of MSE, integrated from 1000 to 700 hPa. From Fig. 12, a number of consistencies emerge across all the datasets, 1) the WA is a convectively unstable region, as the MSE profile weakens with the elevation; 2) in the Sahel region, the convection is initiated by strong instability in the lower layers (<800 hPa) where the availability of MSE and specific humidity (Fig. S11) is high; 3) there is also agreement that, conversely, stronger instability (high MSE) is not conducive to high rainfall, as wetter experiments (coupled runs) simulate weaker MSE compared to drier experiments (atmosphere-only runs), with a REMO minus ROM mean difference > 0.50 kJ kg^{-1} for reanalysis-forced runs and >0.90 kJ kg^{-1} for the ESM-forced runs. However, REMO-MPI, which was found to be moister over the Guinea Coast than ROM-MPI, also simulates a stronger MSE over the Guinea Coast, with a difference in REMO minus ROM > 3.70 kJ kg^{-1}. Moreover, REMO-ERA and ROM-ERA, displaying nearly equal rainfall amounts over this region, also simulate similar MSE with a REMO minus ROM difference < 0.50 kJ kg^{-1}. This suggests that over the Guinea Coast, strong MSE indeed leads to strong precipitation. The LSE (Fig. S12) appears to be the component linking MSE and precipitation, as the overall datasets mirror similar variations in DSE (Fig. S13). The surplus of low-level moisture content, originating from the WAWJ and the northward low-level cross-northern border Guinea Coast influx (Fig. 7 and Fig. S6), destabilizes the near-surface layers over the Sahel. Simultaneously, radiative cooling resulting from enhanced evaporation (Fig. S5) weakens low-level temperatures, thereby attempting to stabilize the lower layers of the troposphere. Previous studies also reported similar results (Giannini 2010; Patricola and Cook 2007). The weakening in MSE, as modeled by ROM-MPI, agrees with the lowering in equatorial east Atlantic Ocean SSTs, which is associated with the reduction in the advected meridional MSE entering the Sahel via the northern frontier (Hill et al. 2017).

5. Summary and concluding discussion

Preliminary studies (e.g., Paxian et al. 2016) showed that dynamical downscaling of coupled global ocean–regional atmosphere RCMs may enhance the simulation of WAM rainfall. The present study aimed to shed light on how such coupling adds value to WAM rainfall, focusing the analyses on the mean climatology and providing a thorough analysis of the West African monsoon system. We evaluated the processes underlying the calculated added value (AV) of including coupling. Additionally, we aimed at understanding how changes in eastern equatorial Atlantic Ocean SSTs force the WAM system or, alternatively, how prior changes in the WAM system induce potential oceanic responses. To achieve this, we utilized the results of dynamical downscaling at ~25-km horizontal resolution from two versions of the Alfred Wegener Institute (AWI)–GERICS RCM model: the atmosphere-only version REMO and the coupled global ocean–regional atmosphere ROM version. The main findings can be summarized as follows:

1) The results are not sensitive to the reference datasets (CRU TS4.05, GPCC v2020, CHIRPS2, and ERA5). The results are quite similar for the reanalysis-forced runs

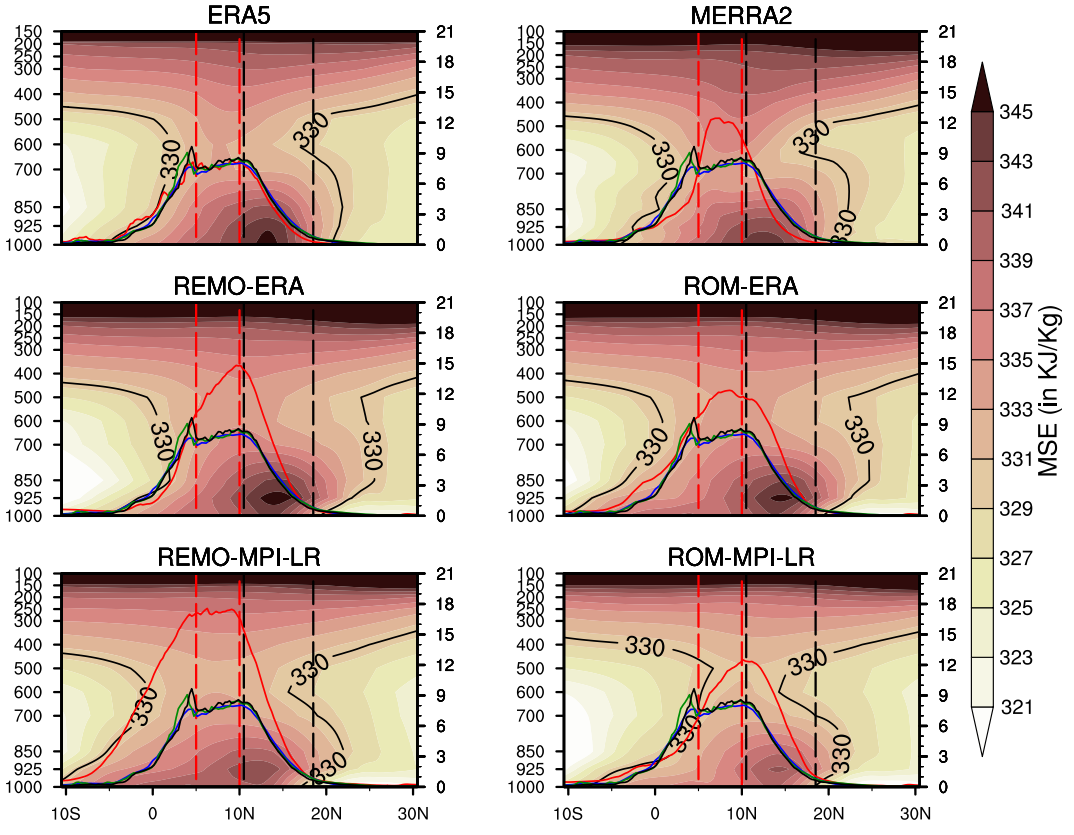

FIG. 12. Latitude–height cross sections of the mean JAS MSE (kJ kg^{-1}). Data used are from reanalysis ERA5 and MERRA-2 datasets and the REMO and ROM experiments over the period 1980–2005. The 330 kJ kg^{-1} contour highlights the potential zone of the convection band. The red line is the latitudinal migration of the rainband (mm day^{-1}) from the dataset under consideration, while the blue, green, and black lines denote the rainband from CRU TS4.05, GPCC v2020, and CHIRPS2 observations. The red bars highlight the latitudinal band of the Guinea Coast (5°–10°N), while the black bars highlight the latitudinal band of the Sahel (10°–20°N).

(REMO-ERA and ROM-ERA), and the strongest differences occur in the ESM-forced experiments (REMO-MPI and ROM-MPI). REMO-ERA and ROM-ERA are wetter than the overall reference data in most parts of WA, while REMO-ERA is slightly drier than ROM-ERA. When driven by MPI-ESM-LR, the spatial pattern of AV consists of a dipole-like structure, with enhancements over much of the Guinea Coast (around 88% ± 2.52%) and a small part of south-central and western Sahel (~10% ± 2.75%), and then degradations over almost half of the Sahel (46% ± 3%). Also, under this mode, REMO and ROM show equivalent performance over 40% ± 3.41% of the Sahel. In this context, REMO and ROM are both moister than the overall reference datasets in most parts of WA, but REMO is wetter (drier) than ROM over the Guinea Coast (Sahel). Additionally, coupling enhances the ITCZ and the WAM rainband intensity and, more broadly, improves the interlinkages between SSTs and monsoon fluxes under ESM-forced conditions compared to reanalysis-forced conditions.

2) Without the influence of biased boundary conditions, ocean coupling exacerbates SST biases over the eastern equatorial Atlantic Ocean, with a knock-on effect on the associated atmospheric fields. However, in the ESM-forced mode, the coupling instead ameliorates the representation of SSTs over this ocean basin, in mitigating the warm SST biases inherited from the driving ESM MPI-ESM-LR.
3) Improvements of the eastern equatorial Atlantic Ocean SSTs lead to improvements in the intensity of monsoon fluxes, achieved through better simulations of evaporation and atmospheric circulation. Indeed, in response to the lowering in warm SST biases, the coupled experiment ROM-MPI also weakens the evaporation over the ocean basin. This leads to decreased amounts of overestimated moisture transported toward the Guinea Gulf, as simulated by the uncoupled REMO-MPI, but still higher compared to ERA5.
4) The coupling also leads to improvements in the representation of land–sea thermal and pressure contrasts (ΔT, ΔP), resulting in enhancements in the simulation of the strength of the monsoon flows. Specifically, the weakening in warm SST biases over the Guinea Gulf strengthens the land–sea thermal contrast and amplifies the pressure contrast between the Sahara and the Guinea Gulf. However, moisture

fluxes entering the Sahel are overestimated due to the higher-than-observed northward low-level cross-northern border Guinea Coast flows, which are related to the stronger surface temperature gradient between 15° and 30°N, and because of the overestimated WAWJ. As a result, the positive ROM-MPI's AV over the Guinea Coast is associated with enhancements in the monsoon flows, but the improvement is mitigated by a stronger moisture divergence across the northern boundary into the Sahel. Conversely, its negative AV over the Sahel is a result of the overestimated moisture convergence from the Guinea Coast and the WAWJ.

5) Coupling improves the representation of the intensity of the midtropospheric (700–600 hPa) and upper-tropospheric (around 200 hPa) circulation. Indeed, the coupled experiment ROM-MPI enhances the magnitude of the AEJ, along with improvements in the intensity and latitudinal positioning of its maintenance mechanism, the SHL. In turn, the SHL is improved in association with the reduction in the magnitude of negative biases in the Saharan radiative budget and the enhancement in the land–sea thermal contrast. The intensity of the TEJ is also significantly enhanced, likely due to a better representation of SSTs in ocean basins that influence the TEJ (Nicholson and Klotter 2020), as modeled by the global ocean model MPIOM. However, the coupling shifts the latitudinal positioning of the jets too far north, which is consistent with increased rainfall over the Sahel leading to negative AV.
6) There is consistency among the overall datasets in terms of convection being triggered in the lower layers of the troposphere (<800 hPa), where the MSE and specific humidity are maximized. Additionally, there is agreement that the LSE is the component of the MSE that plays a crucial role in linking it to precipitation. However, in uncoupled experiments, the modeled MSE over the Sahel is stronger in comparison with the corresponding coupled simulations. Conversely, in coupled runs, the Sahel experiences more rainfall than in uncoupled runs. This suggests that convection in the Sahel is associated with moderate instability. A similar analysis conducted over the Guinea Coast shows that higher instability, on the other hand, leads to stronger ascent motions, consequently resulting in increased precipitation. As simulated by the coupled experiment ROM-MPI, it is logical that the overestimated evaporation over most parts of the Sahel contributes to increased radiative cooling through the evaporative cooling due to a larger latent heat flux, thereby strengthening the stability of the lower layers through a weakening in temperature at those levels. Similarly, the MSE may also weaken in response to the reduction in equatorial east Atlantic Ocean SSTs, presumably inducing a decrease in the advected meridional MSE entering the Sahel through its northern boundary.
7) Compared to their atmosphere-only counterparts, the coupled experiments exhibit a stronger surface temperature gradient, located around 20°N for ROM-ERA and within the latitude band of 15°–30°N for ROM-MPI. Proportionally, these thermal gradients are responsible for stronger moisture advection into the Sahel when compared not only to their respective uncoupled counterparts but also in relation to reanalyses. The strength of this surface temperature gradient drives the northward extent of the WAM rainband as it defines the depth of inland penetration of monsoon fluxes. Consequently, the latitudinal positioning of the WAM convective system is determined by the force of this surface thermal gradient, which, in turn, controls the intensity of convective activities and the strength of monsoon flows. Thus, the monsoon fluxes can be understood as a product of the WAM convective system. In other words, while the reversal in the land–sea thermal contrast triggers the monsoon fluxes over the ocean basin, it is the surface temperature gradient between the Sahara and the Sahel that maintains inflows toward the Sahel, thereby regulating the amount and depth of inland moisture convergence. Similar conclusions were reached by Birch et al. (2014) using explicit simulations. These authors demonstrated that convective activity forces the monsoon winds through the pressure gradient between the Guinea Coast and the Sahel, in association with low pressure in the Sahel. These conditions are favored by the intensification of the SHL as modeled by ROM-MPI compared to REMO-MPI.

The present study further demonstrates the need of simulating monsoon systems using climate models that consider all Earth system components involved. Indeed, these findings show that under certain conditions, significant biases in large-scale processes can obscure local/regional factors, which have a predominant imprint on the local/regional climate system. For instance, excessively warm modeled SSTs over the Guinea Gulf tend to hide the surface thermal gradient between 15° and 30°N, which is responsible for sustaining monsoon flows. This argument is even more valid since compared to the reanalysis ERA5, the coupled ROM-MPI run has significantly improved the representativeness of this surface thermal gradient, unlike the atmosphere-only REMO-MPI run. Whether we elucidated the reason behind the stronger-than-actual northward low-level cross-northern border Guinea Coast moisture fluxes toward the Sahel, as modeled by the coupled experiment ROM-MPI, the causes of overestimated moisture originating from the WAWJ are still lacking and will prompt forthcoming research.

It is worth noting that the robustness of these results must be further assessed since our study focuses only on the results of a single dynamically downscaled ESM through an RCM in both its coupled and uncoupled configurations. Further analyses should involve other RCMs in both configurations, forced with different ESMs. However, we advocate in advance for the greater reliability of the coupled model, ROM, over the uncoupled model, REMO. ROM has demonstrated advantages in modeling other monsoon systems such as the East Asian summer monsoon (Zhu et al. 2020), CORDEX Central America (Cabos et al. 2019), Central Africa (Weber et al. 2023; Tamoffo et al. 2024), and northern North Atlantic and Europe (Sein et al. 2015). Likewise, comparing REMO and ROM forced by the AMIP and CMIP versions of MPI-ESM

could provide further insight into the impact of coupling on the simulation of the WAM. These experiments will allow for a few decades of spinup, reducing possible differences related to the spinup time length. In this regard, ERA5, which extends back to 1940, could also be utilized.

Acknowledgments. The research of this article was supported by the Humboldt-Stiftung as part of the Humboldt Research Fellowship for researchers of all nationalities and research areas: postdoctoral and experienced researchers program. The Helmholtz-Zentrum Hereon has funded the open access. The model simulations were performed at the German Climate Computing Center [Deutsches Klimarechenzentrum (DKRZ)] in Hamburg, with the support of the Climate Service Center Germany (GERICS). We acknowledge all the reanalysis, satellite, and observational data providers used in this study. The helpful input of Peter Hoffmann was also really appreciated. The authors thank the three anonymous reviewers and the editor whose comments helped improve and clarify this manuscript. The authors declare no conflicts of interest relevant to this study.

Data availability statement. The model simulations were performed at the German Climate Computing Center [Deutsches Klimarechenzentrum (DKRZ)] in Hamburg. All observational and reanalysis data used in this study are publicly available at no charge and with unrestricted access. The ERA5 reanalysis is produced within the Copernicus Climate Change Service (C3S) by the ECMWF and is accessible via the link https://cds.climate.copernicus.eu/cdsapp#!/dataset/reanalysis-era5-pressure-levels-monthly-means?tab1/4form; the MERRA-2 reanalysis, developed by the NASA, is available online (at https://disc.gsfc.nasa.gov/datasets?keywords1/4%22MERRA-2%22&page1/41&source1/4Models%2FAnalyses%20MERRA-2). The GPCC observational dataset is available at https://opendata.dwd.de/climate_environment/GPCC/html/fulldata-monthly_v2020_doi_download.html. The CRU-v4.04 dataset is available at https://data.ceda.ac.uk/badc/cru/data/cru_ts/cru_ts_4.05/data/pre (UEA 2019); the CHIRPS2 data are available at https://data.chc.ucsb.edu/products/CHIRPS-2.0/global_daily/netcdf/.

REFERENCES

Akinsanola, A. A., and W. Zhou, 2019: Projections of West African summer monsoon rainfall extremes from two CORDEX models. *Climate Dyn.*, **52**, 2017–2028, https://doi.org/10.1007/s00382-018-4238-8.

——, V. O. Ajayi, A. T. Adejare, O. E. Adeyeri, I. E. Gbode, K. O. Ogunjobi, G. Nikulin, and A. T. Abolude, 2018: Evaluation of rainfall simulations over West Africa in dynamically downscaled CMIP5 global circulation models. *Theor. Appl. Climatol.*, **132**, 437–450, https://doi.org/10.1007/s00704-017-2087-8.

Biasutti, M., 2019: Rainfall trends in the African Sahel: Characteristics, processes, and causes. *Wiley Interdiscip. Rev.: Climate Change*, **10**, e591, https://doi.org/10.1002/wcc.591.

——, A. H. Sobel, and S. J. Camargo, 2009: The role of the Sahara low in summertime Sahel rainfall variability and change in the CMIP3 models. *J. Climate*, **22**, 5755–5771, https://doi.org/10.1175/2009JCLI2969.1.

Bichet, A., A. Diedhiou, B. Hingray, G. Evin, N. E. Touré, K. N. A. Browne, and K. Kouadio, 2020: Assessing uncertainties in the regional projections of precipitation in CORDEX AFRICA. *Climatic Change*, **162**, 583–601, https://doi.org/10.1007/s10584-020-02833-z.

Birch, C. E., D. J. Parker, J. H. Marsham, D. Copsey, and L. Garcia-Carreras, 2014: A seamless assessment of the role of convection in the water cycle of the West African Monsoon. *J. Geophys. Res. Atmos.*, **119**, 2890–2912, https://doi.org/10.1002/2013JD020887.

Boone, A., and Coauthors, 2009: The AMMA land surface model Intercomparison Project (ALMIP). *Bull. Amer. Meteor. Soc.*, **90**, 1865–1880, https://doi.org/10.1175/2009BAMS2786.1.

Boone, A. A., I. Poccard-Leclercq, Y. Xue, J. Feng, and P. de Rosnay, 2010: Evaluation of the WAMME model surface fluxes using results from the AMMA land-surface model intercomparison project. *Climate Dyn.*, **35**, 127–142, https://doi.org/10.1007/s00382-009-0653-1.

Cabos, W., and Coauthors, 2017: The South Atlantic anticyclone as a key player for the representation of the tropical Atlantic climate in coupled climate models. *Climate Dyn.*, **48**, 4051–4069, https://doi.org/10.1007/s00382-016-3319-9.

——, and Coauthors, 2019: Dynamical downscaling of historical climate over CORDEX Central America domain with a regionally coupled atmosphere–ocean model. *Climate Dyn.*, **52**, 4305–4328, https://doi.org/10.1007/s00382-018-4381-2.

——, A. de la Vara, F. J. Álvarez-García, E. Sánchez, K. Sieck, J.-I. Pérez-Sanz, N. Limareva, and D. V. Sein, 2020: Impact of ocean-atmosphere coupling on regional climate: The Iberian Peninsula case. *Climate Dyn.*, **54**, 4441–4467, https://doi.org/10.1007/s00382-020-05238-x.

Chauvin, F., R. Roehrig, and J.-P. Lafore, 2010: Intraseasonal variability of the Saharan heat low and its link with midlatitudes. *J. Climate*, **23**, 2544–2561, https://doi.org/10.1175/2010JCLI3093.1.

Chen, T.-C., 2005: Maintenance of the midtropospheric North African summer circulation: Saharan high and African easterly jet. *J. Climate*, **18**, 2943–2962, https://doi.org/10.1175/JCLI3446.1.

Cook, K. H., 1999: Generation of the African easterly jet and its role in determining West African precipitation. *J. Climate*, **12**, 1165–1184, https://doi.org/10.1175/1520-0442(1999)012<1165:GOTAEJ>2.0.CO;2.

——, and E. K. Vizy, 2006: Coupled model simulations of the West African monsoon system: Twentieth- and twenty-first-century simulations. *J. Climate*, **19**, 3681–3703, https://doi.org/10.1175/JCLI3814.1.

Dee, D. P., and Coauthors, 2011: The ERA-Interim reanalysis: Configuration and performance of the data assimilation system. *Quart. J. Roy. Meteor. Soc.*, **137**, 553–597, https://doi.org/10.1002/qj.828.

Diallo, I., C. L. Bain, A. T. Gaye, W. Moufouma-Okia, C. Niang, M. D. B. Dieng, and R. Graham, 2014: Simulation of the West African monsoon onset using the HadGEM3-RA regional climate model. *Climate Dyn.*, **43**, 575–594, https://doi.org/10.1007/s00382-014-2219-0.

——, F. Giorgi, A. Deme, M. Tall, L. Mariotti, and A. T. Gaye, 2016: Projected changes of summer monsoon extremes and hydroclimatic regimes over West Africa for the twenty-first century. *Climate Dyn.*, **47**, 3931–3954, https://doi.org/10.1007/s00382-016-3052-4.

Diedhiou, A., S. Janicot, A. Viltard, P. de Felice, and H. Laurent, 1999: Easterly wave regimes and associated convection over West Africa and tropical Atlantic: Results from the NCEP/NCAR and ECMWF reanalyses. *Climate Dyn.*, **15**, 795–822, https://doi.org/10.1007/s003820050316.

Dixon, R. D., A. S. Daloz, D. J. Vimont, and M. Biasutti, 2017: Saharan heat low biases in CMIP5 models. *J. Climate*, **30**, 2867–2884, https://doi.org/10.1175/JCLI-D-16-0134.1.

Doblas-Reyes, F. J., and Coauthors, 2021: Linking global to regional climate change. *Climate Change 2021: The Physical Science Basis*. V. P. Masson-Delmotte et al., Eds., Cambridge University Press, 1363–1512, https://doi.org/10.1017/9781009157896.012.

d'Orgeval, T., 2008: Impact du changement climatique sur la saison des pluies en Afrique de l'Ouest: Que nous disent les modèles de climat actuels? *Sci. Changements Planét./Sécheresse*, **19**, 79–85.

Dosio, A., H.-J. Panitz, M. Schubert-Frisius, and D. Lüthi, 2015: Dynamical downscaling of CMIP5 global circulation models over CORDEX-Africa with COSMO-CLM: Evaluation over the present climate and analysis of the added value. *Climate Dyn.*, **44**, 2637–2661, https://doi.org/10.1007/s00382-014-2262-x.

——, and Coauthors, 2020: A tale of two futures: Contrasting scenarios of future precipitation for West Africa from an ensemble of regional climate models. *Environ. Res. Lett.*, **15**, 064007, https://doi.org/10.1088/1748-9326/ab7fde.

Druyan, L. M., and Coauthors, 2010: The WAMME regional model intercomparison study. *Climate Dyn.*, **35**, 175–192, https://doi.org/10.1007/s00382-009-0676-7.

Engelstaedter, S., R. Washington, C. Flamant, D. J. Parker, C. J. T. Allen, and M. C. Todd, 2015: The Saharan heat low and moisture transport pathways in the central Sahara—Multiaircraft observations and Africa-LAM evaluation. *J. Geophys. Res. Atmos.*, **120**, 4417–4442, https://doi.org/10.1002/2015JD023123.

Eyring, V., S. Bony, G. A. Meehl, C. A. Senior, B. Stevens, R. J. Stouffer, and K. E. Taylor, 2016: Overview of the Coupled Model Intercomparison Project Phase 6 (CMIP6) experimental design and organization. *Geosci. Model Dev.*, **9**, 1937–1958, https://doi.org/10.5194/gmd-9-1937-2016.

Feser, F., 2006: Enhanced detectability of added value in limited-area model results separated into different spatial scales. *Mon. Wea. Rev.*, **134**, 2180–2190, https://doi.org/10.1175/MWR3183.1.

Fontaine, B., N. Philippon, and P. Camberlin, 1999: An improvement of June–September rainfall forecasting in the Sahel based upon region April–May moist static energy content (1968–1997). *Geophys. Res. Lett.*, **26**, 2041–2044, https://doi.org/10.1029/1999GL900495.

Funk, C., and Coauthors, 2015: The climate hazards infrared precipitation with stations—A new environmental record for monitoring extremes. *Sci. Data*, **2**, 150066, https://doi.org/10.1038/sdata.2015.66.

Gbode, I. E., T. E. Babalola, G. T. Diro, and J. D. Intsiful, 2023: Assessment of ERA5 and ERA-Interim in reproducing mean and extreme climates over West Africa. *Adv. Atmos. Sci.*, **40**, 570–586, https://doi.org/10.1007/s00376-022-2161-8.

Giannini, A., 2010: Mechanisms of climate change in the semiarid African Sahel: The local view. *J. Climate*, **23**, 743–756, https://doi.org/10.1175/2009JCLI3123.1.

——, S. Salack, T. Lodoun, A. Ali, A. T. Gaye, and O. Ndiaye, 2013: A unifying view of climate change in the Sahel linking intra-seasonal, interannual and longer time scales. *Environ. Res. Lett.*, **8**, 024010, https://doi.org/10.1088/1748-9326/8/2/024010.

Gibba, P., M. B. Sylla, E. C. Okogbue, A. T. Gaye, M. Nikiema, and I. Kebe, 2019: State-of-the-art climate modeling of extreme precipitation over Africa: Analysis of CORDEX added-value over CMIP5. *Theor. Appl. Climatol.*, **137**, 1041–1057, https://doi.org/10.1007/s00704-018-2650-y.

Gutowski, W. J., Jr., and Coauthors, 2016: WCRP COordinated Regional Downscaling EXperiment (CORDEX): A diagnostic MIP for CMIP6. *Geosci. Model Dev.*, **9**, 4087–4095, https://doi.org/10.5194/gmd-9-4087-2016.

Harris, I., T. J. Osborn, P. Jones, and D. Lister, 2020: Version 4 of the CRU TS monthly high-resolution gridded multivariate climate dataset. *Sci. Data*, **7**, 109, https://doi.org/10.1038/s41597-020-0453-3.

Hersbach, H., and Coauthors, 2020: The ERA5 global reanalysis. *Quart. J. Roy. Meteor. Soc.*, **146**, 1999–2049, https://doi.org/10.1002/qj.3803.

Hill, S. A., Y. Ming, I. M. Held, and M. Zhao, 2017: A moist static energy budget based analysis of the Sahel rainfall response to uniform oceanic warming. *J. Climate*, **30**, 5637–5660, https://doi.org/10.1175/JCLI-D-16-0785.1.

Hourdin, F., and Coauthors, 2010: AMMA-Model Intercomparison Project. *Bull. Amer. Meteor. Soc.*, **91**, 95–104, https://doi.org/10.1175/2009BAMS2791.1.

Hwang, Y.-T., D. M. W. Frierson, and S. M. Kang, 2013: Anthropogenic sulfate aerosol and the southward shift of tropical precipitation in the late 20th century. *Geophys. Res. Lett.*, **40**, 2845–2850, https://doi.org/10.1002/grl.50502.

Jacob, D., 2001: The role of water vapour in the atmosphere. A short overview from a climate modeller's point of view. *Phys. Chem. Earth*, **26**, 523–527, https://doi.org/10.1016/S1464-1895(01)00094-1.

——, and R. Podzun, 1997: Sensitivity studies with the regional climate model REMO. *Meteor. Atmos. Phys.*, **63**, 119–129, https://doi.org/10.1007/BF01025368.

——, and Coauthors, 2012: Assessing the transferability of the regional climate model REMO to different COordinated Regional climate Downscaling EXperiment (CORDEX) regions. *Atmosphere*, **3**, 181–199, https://doi.org/10.3390/atmos3010181.

Janicot, S., V. Moron, and B. Fontaine, 1996: Sahel droughts and ENSO dynamics. *Geophys. Res. Lett.*, **23**, 515–518, https://doi.org/10.1029/96GL00246.

Jungclaus, J. H., and Coauthors, 2013: Characteristics of the ocean simulations in the Max Planck Institute Ocean Model (MPIOM) the ocean component of the MPI-Earth system model. *J. Adv. Model. Earth Syst.*, **5**, 422–446, https://doi.org/10.1002/jame.20023.

Kiladis, G. N., C. D. Thorncroft, and N. M. J. Hall, 2006: Three-dimensional structure and dynamics of African easterly waves. Part I: Observations. *J. Atmos. Sci.*, **63**, 2212–2230, https://doi.org/10.1175/JAS3741.1.

Koteswaram, P., 1958: The easterly jet stream in the Tropics. *Tellus*, **10**, 43–57, https://doi.org/10.1111/j.2153-3490.1958.tb01984.x.

Laprise, R., L. Hernández-Díaz, K. Tete, L. Sushama, L. Šeparović, A. Martynov, K. Winger, and M. Valin, 2013: Climate projections over CORDEX Africa domain using the fifth-generation Canadian Regional Climate Model (CRCM5). *Climate Dyn.*, **41**, 3219–3246, https://doi.org/10.1007/s00382-012-1651-2.

Lavaysse, C., 2015: Saharan desert warming. *Nat. Climate Change*, **5**, 807–808, https://doi.org/10.1038/nclimate2773.

——, C. Flamant, S. Janicot, D. J. Parker, J.-P. Lafore, B. Sultan, and J. Pelon, 2009: Seasonal evolution of the West African heat low: A climatological perspective. *Climate Dyn.*, **33**, 313–330, https://doi.org/10.1007/s00382-009-0553-4.

——, ——, and ——, 2010: Regional-scale convection patterns during strong and weak phases of the Saharan heat low. *Atmos. Sci. Lett.*, **11**, 255–264, https://doi.org/10.1002/asl.284.

——, J.-P. Chaboureau, and C. Flamant, 2011: Dust impact on the West African heat low in summertime. *Quart. J. Roy. Meteor. Soc.*, **137**, 1227–1240, https://doi.org/10.1002/qj.844.

Lemburg, A., J. Bader, and M. Claussen, 2019: Sahel rainfall–tropical easterly jet relationship on synoptic to intraseasonal time scales. *Mon. Wea. Rev.*, **147**, 1733–1752, https://doi.org/10.1175/MWR-D-18-0254.1.

Leroux, S., and N. M. J. Hall, 2009: On the relationship between African easterly waves and the African easterly jet. *J. Atmos. Sci.*, **66**, 2303–2316, https://doi.org/10.1175/2009JAS2988.1.

Martin, E. R., and C. D. Thorncroft, 2014: The impact of the AMO on the West African monsoon annual cycle. *Quart. J. Roy. Meteor. Soc.*, **140**, 31–46, https://doi.org/10.1002/qj.2107.

Meehl, G. A., C. Covey, T. Delworth, M. Latif, B. McAvaney, J. F. B. Mitchell, R. J. Stouffer, and K. E. Taylor, 2007: THE WCRP CMIP3 multimodel dataset: A new era in climate change research. *Bull. Amer. Meteor. Soc.*, **88**, 1383–1394, https://doi.org/10.1175/BAMS-88-9-1383.

Monerie, P.-A., P. Roucou, and B. Fontaine, 2013: Mid-century effects of climate change on African monsoon dynamics using the A1B emission scenario. *Int. J. Climatol.*, **33**, 881–896, https://doi.org/10.1002/joc.3476.

——, C. M. Wainwright, M. Sidibe, and A. A. Akinsanola, 2020: Model uncertainties in climate change impacts on Sahel precipitation in ensembles of CMIP5 and CMIP6 simulations. *Climate Dyn.*, **55**, 1385–1401, https://doi.org/10.1007/s00382-020-05332-0.

——, L. J. Wilcox, and A. G. Turner, 2022: Effects of anthropogenic aerosol and greenhouse gas emissions on Northern Hemisphere monsoon precipitation: Mechanisms and uncertainty. *J. Climate*, **35**, 2305–2326, https://doi.org/10.1175/JCLI-D-21-0412.1.

NASA, 2016: Modern-Era Retrospective Analysis for Research and Applications, version 2. Goddard Earth Sciences Data and Information Services Center, accessed 12 September 2017, https://disc.gsfc.nasa.gov/daac-bin/FTPSubset.pl.

Nesbitt, S. W., R. Cifelli, and S. A. Rutledge, 2006: Storm morphology and rainfall characteristics of TRMM precipitation features. *Mon. Wea. Rev.*, **134**, 2702–2721, https://doi.org/10.1175/MWR3200.1.

Niang, I., O. C. Ruppel, M. A. Abdrabo, A. Essel, C. Lennard, J. Padgham, and P. Urquhart, 2014: Africa. *Climate Change 2014: Impacts, Adaptation, and Vulnerability. Part B: Regional Aspects*, V. R. Barros et al., Eds., Cambridge University Press, 1199–1265, https://www.ipcc.ch/site/assets/uploads/2018/02/WGIIAR5PartB_FINAL.pdf.

Nicholson, S. E., 2013: The West African Sahel: A review of recent studies on the rainfall regime and its interannual variability. *ISRN Meteor.*, **2013**, 453521, https://doi.org/10.1155/2013/453521.

——, and J. P. Grist, 2003: The seasonal evolution of the atmospheric circulation over West Africa and equatorial Africa. *J. Climate*, **16**, 1013–1030, https://doi.org/10.1175/1520-0442(2003)016<1013:TSEOTA>2.0.CO;2.

——, and D. Klotter, 2020: The tropical easterly jet over Africa, its representation in six reanalysis products, and its association with Sahel rainfall. *Int. J. Climatol.*, **41**, 328–347, https://doi.org/10.1002/joc.6623.

——, ——, L. Zhou, and W. Hua, 2019: Validation of satellite precipitation estimates over the Congo Basin. *J. Hydrometeor.*, **20**, 631–656, https://doi.org/10.1175/JHM-D-18-0118.1.

Paeth, H., and B. Mannig, 2012: On the added value of regional climate modeling in climate change assessment. *Climate Dyn.*, **41**, 1057–1066, http://doi.org/10.1007/s00382-012-1517-7.

——, K. Born, R. Podzun, and D. Jacob, 2005: Regional dynamical downscaling over West Africa: Model evaluation and comparison of wet and dry years. *Meteor. Z.*, **14**, 349–367, https://doi.org/10.1127/0941-2948/2005/0038.

Panitz, H.-J., A. Dosio, M. Büchner, D. Lüthi, and K. Keuler, 2014: COSMO-CLM (CCLM) climate simulations over CORDEX-Africa domain: Analysis of the ERA-Interim driven simulations at 0.44° and 0.22° resolution. *Climate Dyn.*, **42**, 3015–3038, https://doi.org/10.1007/s00382-013-1834-5.

Parker, D. J., and Coauthors, 2005: The diurnal cycle of the West African monsoon circulation. *Quart. J. Roy. Meteor. Soc.*, **131**, 2839–2860, https://doi.org/10.1256/qj.04.52.

Patricola, C. M., and K. H. Cook, 2007: Dynamics of the West African monsoon under mid-Holocene precessional forcing: Regional climate model simulations. *J. Climate*, **20**, 694–716, https://doi.org/10.1175/JCLI4013.1.

Paxian, A., and Coauthors, 2016: Bias reduction in decadal predictions of West African monsoon rainfall using regional climate models. *J. Geophys. Res. Atmos.*, **121**, 1715–1735, https://doi.org/10.1002/2015JD024143.

Pu, B., and K. H. Cook, 2010: Dynamics of the West African westerly jet. *J. Climate*, **23**, 6263–6276, https://doi.org/10.1175/2010JCLI3648.1.

——, and ——, 2012: Role of the West African westerly jet in Sahel rainfall variations. *J. Climate*, **25**, 2880–2896, https://doi.org/10.1175/JCLI-D-11-00394.1.

Quagraine, K. A., F. Nkrumah, C. Klein, N. A. B. Klutse, and K. T. Quagraine, 2020: West African summer monsoon precipitation variability as represented by reanalysis datasets. *Climate*, **8**, 111, https://doi.org/10.3390/cli8100111.

Ratnam, J. V., Y. Morioka, S. K. Behera, and T. Yamagata, 2015: A model study of regional air-sea interaction in the austral summer precipitation over southern Africa. *J. Geophys. Res. Atmos.*, **120**, 2342–2357, https://doi.org/10.1002/2014JD022154.

Redelsperger, J.-L., C. D. Thorncroft, A. Diedhiou, T. Lebel, D. J. Parker, and J. Polcher, 2006: African monsoon multidisciplinary analysis: An international research project and field campaign. *Bull. Amer. Meteor. Soc.*, **87**, 1739–1746, https://doi.org/10.1175/BAMS-87-12-1739.

Rodríguez-Fonseca, B., and Coauthors, 2015: Variability and predictability of West African droughts: A review on the role of sea surface temperature anomalies. *J. Climate*, **28**, 4034–4060, https://doi.org/10.1175/JCLI-D-14-00130.1.

Saini, R., G. Wang, M. Yu, and J. Kim, 2015: Comparison of RCM and GCM projections of boreal summer precipitation over Africa. *J. Geophys. Res. Atmos.*, **120**, 3679–3699, https://doi.org/10.1002/2014JD022599.

Samanta, D., S. N. Hameed, D. Jin, V. Thilakan, M. Ganai, S. A. Rao, and M. Deshpande, 2018: Impact of a narrow coastal Bay of Bengal sea surface temperature front on an Indian summer monsoon simulation. *Sci. Rep.*, **8**, 17694, https://doi.org/10.1038/s41598-018-35735-3.

Schepanski, K., B. Heinold, and I. Tegen, 2017: Harmattan, Saharan heat low, and West African monsoon circulation: Modulations on the Saharan dust outflow towards the North Atlantic. *Atmos. Chem. Phys.*, **17**, 10 223–10 243, https://doi.org/10.5194/acp-17-10223-2017.

Schneider, U., S. Hänsel, P. Finger, E. Rustemeier, and M. Ziese, 2022: GPCC full data monthly product version 2022 at 0.25°: Monthly land-surface precipitation from rain-gauges built on GTS-based and historical data. Accessed 3 June 2023, https://doi.org/10.5676/DWD_GPCC/FD_M_V2022_025.

Sein, D. V., N. V. Koldunov, J. G. Pinto, and W. Cabos, 2014: Sensitivity of simulated regional Arctic climate to the choice of coupled model domain. *Tellus*, **66A**, 23966, https://doi.org/10.3402/tellusa.v66.23966.

——, and Coauthors, 2015: Regionally coupled atmosphere-ocean-sea ice-marine biogeochemistry model ROM: 1. Description and validation. *J. Adv. Model. Earth Syst.*, **7**, 268–304, https://doi.org/10.1002/2014MS000357.

Song, F., L. R. Leung, J. Lu, and L. Dong, 2018: Seasonally dependent responses of subtropical highs and tropical rainfall to anthropogenic warming. *Nat. Climate Change*, **8**, 787–792, https://doi.org/10.1038/s41558-018-0244-4.

Stevens, B., and Coauthors, 2013: Atmospheric component of the MPI-M Earth System Model: ECHAM6. *J. Adv. Model. Earth Syst.*, **5**, 146–172, https://doi.org/10.1002/jame.20015.

Sultan, B., and S. Janicot, 2003: The West African monsoon dynamics. Part II: The "preonset" and "onset" of the Summer Monsoon. *J. Climate*, **16**, 3407–3427, https://doi.org/10.1175/1520-0442(2003)016<3407:TWAMDP>2.0.CO;2.

Tamoffo, A. T., A. Dosio, D. A. Vondou, and D. Sonkoué, 2020: Process-based analysis of the added value of dynamical downscaling over central Africa. *Geophys. Res. Lett.*, **47**, e2020GL089702, https://doi.org/10.1029/2020GL089702.

——, ——, L. K. Amekudzi, and T. Weber, 2023a: Process-oriented evaluation of the West African Monsoon system in CORDEX-CORE regional climate models. *Climate Dyn.*, **60**, 3187–3210, https://doi.org/10.1007/s00382-022-06502-y.

——, A. A. Akinsanola, and T. Weber, 2023b: Understanding the diversity of the West African Monsoon system change projected by CORDEX-CORE regional climate models. *Climate Dyn.*, **61**, 2395–2419, https://doi.org/10.1007/s00382-023-06690-1.

——, T. Weber, W. Cabos, D. V. Sein, A. Dosio, D. Rechid, A. R. Remrdio, and D. Jacob, 2024: Mechanisms of added value of a coupled global ocean-regional atmosphere climate model over central equatorial Africa. *J. Geophys. Res. Atmos.*, **129**, e2023JD039385, https://doi.org/10.1029/2023JD039385.

Taylor, K. E., R. J. Stouffer, and G. A. Meehl, 2012: An overview of CMIP5 and the experiment design. *Bull. Amer. Meteor. Soc.*, **93**, 485–498, https://doi.org/10.1175/BAMS-D-11-00094.1.

Thorncroft, C. D., and M. Blackburn, 1999: Maintenance of the African easterly jet. *Quart. J. Roy. Meteor. Soc.*, **125**, 763–786, https://doi.org/10.1002/qj.49712555502.

——, and Coauthors, 2003: The JET2000 project: Aircraft observations of the African easterly jet and African easterly waves. *Bull. Amer. Meteor. Soc.*, **84**, 337–352, https://doi.org/10.1175/BAMS-84-3-337.

——, N. M. J. Hall, and G. N. Kiladis, 2008: Three-dimensional structure and dynamics of African easterly waves. Part III: Genesis. *J. Atmos. Sci.*, **65**, 3596–3607, https://doi.org/10.1175/2008JAS2575.1.

Vizy, E. K., and K. H. Cook, 2002: Development and application of a mesoscale climate model for the tropics: Influence of sea surface temperature anomalies on the West African monsoon. *J. Geophys. Res.*, **107**, 4023, https://doi.org/10.1029/2001JD000686.

——, and ——, 2009: A mechanism for African monsoon breaks: Mediterranean cold air surges. *J. Geophys. Res.*, **114**, D01104, https://doi.org/10.1029/2008JD010654.

——, ——, J. Crétat, and N. Neupane, 2013: Projections of a wetter Sahel in the twenty-first century from global and regional models. *J. Climate*, **26**, 4664–4687, https://doi.org/10.1175/JCLI-D-12-00533.1.

Weber, T., W. Cabos, D. V. Sein, and D. Jacob, 2023: Benefits of simulating precipitation characteristics over Africa with a regionally-coupled atmosphere–ocean model. *Climate Dyn.*, **60**, 1079–1102, https://doi.org/10.1007/s00382-022-06329-7.

Whittleston, D., S. E. Nicholson, A. Schlosser, and D. Entekhabi, 2017: Climate models lack jet–rainfall coupling over West Africa. *J. Climate*, **30**, 4625–4632, https://doi.org/10.1175/JCLI-D-16-0579.1.

Wu, M., G. Nikulin, E. Kjellström, D. Belušić, C. Jones, and D. Lindstedt, 2020: The impact of regional climate model formulation and resolution on simulated precipitation in Africa. *Earth Syst. Dyn.*, **11**, 377–394, https://doi.org/10.5194/esd-11-377-2020.

Xue, Y., and Coauthors, 2010: Intercomparison and analyses of the climatology of the West African monsoon in the West African Monsoon Modeling and Evaluation project (WAMME) first model intercomparison experiment. *Climate Dyn.*, **35**, 3–27, https://doi.org/10.1007/s00382-010-0778-2.

Zhao, Y., and Coauthors, 2005: A multi-model analysis of the role of the ocean on the African and Indian monsoon during the mid-Holocene. *Climate Dyn.*, **25**, 777–800, https://doi.org/10.1007/s00382-005-0075-7.

Zhou, T., J. Lu, W. Zhang, and Z. Chen, 2020: The sources of uncertainty in the projection of global land monsoon precipitation. *Geophys. Res. Lett.*, **47**, e2020GL088415, https://doi.org/10.1029/2020GL088415.

Zhu, S., and Coauthors, 2020: Added value of the regionally coupled model ROM in the East Asian summer monsoon modeling. *Theor. Appl. Climatol.*, **140**, 375–387, https://doi.org/10.1007/s00704-020-03093-8.

Zou, L., and T. Zhou, 2016: A regional ocean–atmosphere coupled model developed for CORDEX East Asia: Assessment of Asian summer monsoon simulation. *Climate Dyn.*, **47**, 3627–3640, https://doi.org/10.1007/s00382-016-3032-8.